INTERNATIONAL JOURNAL FOR NUMERICAL METHODS IN FLUIDS
Int. J. Numer. Meth. Fluids 2016; **80**:397–428
Published online 3 September 2015 in Wiley Online Library (wileyonlinelibrary.com). DOI: 10.1002/fld.4086

An adaptive finite element method for the modeling of the equilibrium of red blood cells

Aymen Laadhari[1,*,†], Pierre Saramito[2] and Chaouqi Misbah[3]

[1]*Computer Vision Laboratory, Institute für Bildverarbeitung, Department of Information Technology and Electrical Engineering, Swiss Federal Institute of Technology – ETHZ, CH-8092 Zürich, Switzerland*
[2]*Laboratoire Jean Kuntzmann, Informatique et Mathématiques Appliquées de Grenoble, Université Joseph Fourier and Centre National de la Recherche Scientifique, F-38041 Grenoble, France*
[3]*Laboratoire Interdisciplinaire de Physique, Université Joseph Fourier and Centre National de la Recherche Scientifique, F-38041 Grenoble, France*

SUMMARY

This contribution is concerned with the numerical modeling of an isolated red blood cell (RBC), and more generally of phospholipid membranes. We propose an adaptive Eulerian finite element approximation, based on the level set method, of a shape optimization problem arising in the study of RBCs. We simulate the equilibrium shapes that minimize the elastic bending energy under prescribed constraints of fixed volume and surface area. An anisotropic mesh adaptation technique is used in the vicinity of the cell membrane to enhance the robustness of the method. Efficient time and spatial discretizations are considered and implemented. We address in detail the main features of the proposed method, and finally we report several numerical experiments in the two-dimensional and the three-dimensional axisymmetric cases. The effectiveness of the numerical method is further demonstrated through numerical comparisons with *semi-analytical* solutions provided by a reduced order model. Copyright © 2015 John Wiley & Sons, Ltd.

Received 22 September 2014; Revised 17 July 2015; Accepted 20 July 2015

KEY WORDS: finite element method; adaptive mesh refinement; minimization under constraints; shape optimization; red blood cell; Canham–Helfrich model

1. INTRODUCTION

The blood represents an essential element for life. It is composed of several cell types that possess specific functions. In particular, red blood cell (RBCs) are the most abundant cells in the blood and allow to carry oxygen through the body. Advancing the modeling strategies and the computational methodologies of the blood function can certainly be a key component in the understanding of blood disorders and the development of novel therapies and prognostic methods. Since several decades, there is an increasing interest in many aspects of blood modeling driven by the increasing demand from the medical community for scientifically rigorous studies of blood. Scientifical investigations extend to a wide range of spatio-temporal scales covering the microscopic and the macroscopic scales. In the present work, we are interested in the microscopic modeling of RBCs. Vesicles, also called liposomes, represent a simple and attractive model introduced to mimic the viscoelastic and the mechanical behaviors of RBCs. They are closed membranes having the structure of amphiphilic molecules that are self-assembled in water to build a structure of bilayers. Regarding the modeling of RBCs and vesicles, several investigations and substantial achievements have been made involving researchers from diverse communities in the fields of biology [1], applied mathematics [2–6],

*Correspondence to: Aymen Laadhari, Computer Vision Laboratory, Institut für Bildverarbeitung, Department of Information Technology and Electrical Engineering, Swiss Federal Institute of Technology - ETHZ, CH-8092 Zürich, Switzerland.
†E-mail: laadhari@vision.ee.ethz.ch

scientific computing [7–9], and the biomedical field [10]. These cells exhibit a wide and rich set of shapes in various physical environments. Effective mathematical models, seconded by the use of accurate numerical methodologies, are needed to study, in particular, the equilibrium shapes of RBCs.

A wide variety of models were developed to describe the deformation of RBCs, for example, [4, 5, 11–18]. Because of the incompressibility, the main mode of the deformation of vesicles is bending, and the bending energy describes the cell shapes. In the early 1970s, Canham [19] and Helfrich [20, 21] formalized the physical properties of the cell membrane in a mathematical model, where the cost in the bending energy is given by the curvature of the membrane. Let us define the mean curvature H and the Gauss curvature K, respectively, as the sum and the product of the principle curvatures on the cell membrane. Let $\Omega \in \mathbb{R}^3$ be a bounded domain with smooth boundary Γ that represents the cell membrane. The bending energy, also referred to as the Willmore energy [22, 23], reads

$$\mathcal{J} = \frac{k}{2}\int_\Gamma (H - H_0)^2 \mathrm{d}s + \frac{k_g}{2}\int_\Gamma K \mathrm{d}s,$$

where k and k_g are two constants that represent the bending rigidity and the Gaussian curvature modulus, respectively. In the present work, we assume unit values of k and k_g. The spontaneous curvature H_0 allows to describe the asymmetry effect of the membrane and its surrounding environment, which is caused by inhomogeneities within the structure of the membrane bilayers, see for example, [24]. The spontaneous curvature has no effect on the shape of the cell in the two-dimensional case, whereas the shape shall depend on H_0 in the tridimensional case [25]. We assume that the shape topological gender of the RBC is preserved, because topological changes are energetically disadvantaged, for example, [25–27]. Accordingly, the integral depending on K in $\mathcal{J}$ is disregarded.

The RBC's membrane has special properties that drive the cell dynamics and control the equilibrium shapes. In fact, the membrane remains impermeable, and the cost of the bending deformations is significantly smaller than the cost of stretching or compressing the membrane. The incompressibility of the inner domain of the cell and the inextensibility of the membrane are required. Hence, the equilibrium shapes of RBCs are the minimizers of the energy of Canham and Helfrich under the constraints of fixed volume and surface area. In addition, the shape depends on specific parameters that are obtained by the non-dimensional formulation of the problem. The RBC can be more or less inflated, and the deflation could be due to the thermal expansion of phospholipids or the osmotic effects. Let us introduce the area A_0 and the volume V_0 of the cell. The reduced volume γ is a dimensionless parameter that measures the deflation of the cell. It represents the ratio between the volume of the cell and the volume of a sphere having the same surface area A_0.

$$\gamma = \frac{3V_0}{4\pi} \times \left(\frac{4\pi}{A_0}\right)^{3/2}.$$

Accordingly, γ can range from 0, that is, completely deflated shape, to 1, that is, spherical shape. The human RBC have usually a biconcave disk-like shape with a reduced volume $\gamma \approx 0.64$. However, other shapes are observed by varying γ, such as the stomatocytes, the oblates, and the prolates [28, 29]. In the two-dimensional case, the dimensionless shape parameter is called the reduced area, and it is given by the ratio between the cell area and the area of a circle having the same perimeter as the cell. It reads

$$\gamma = \frac{V_0}{\pi} \times \left(\frac{2\pi}{A_0}\right)^2.$$

The Euler–Lagrange equation describes the equilibrium shapes of RBCs, where two Lagrange multipliers p and σ help to impose the volume and area constraints, respectively. This equation was obtained using various mathematical approaches, such as the differential geometry [30, 31] and the shape differentiation technique [32–34]. In a previous work [34], we derived a generalized mechanical equation describing the RBC's equilibrium:

DOI: 10.1002/fld

$$p + \sigma H + k_c \left(\frac{1}{2}(H - H_0)[4K - H(H + H_0)] - \Delta_s H \right) = 0,$$

where Δ_s represents the Laplace–Beltrami operator.

Several experimental and theoretical studies have focused on the equilibrium shapes of BRCs and vesicles. While there is a substantial interest from the numerical point of view, most of these contributions have used lumped parameter models. Some numerical strategies for the modeling of RBCs shapes in the equilibrium can be found in [1, 4, 26, 35]. According to their framework, RBC models can be roughly divided into two families: Lagrangian models and Eulerian models. On the one hand, in a Lagrangian-based framework, the model is written in the reference configuration. A mesh fitting the RBC's shape is employed and deforms according to the cell motion. Although more precise, the Lagrangian methods are often a demanding task that could generate computational instabilities related to the deterioration of the mesh quality. Sophisticated remeshing strategies are then required. For instance, the boundary element method [36, 37] and the immersed boundary method [38] are widely used. On the other hand, Eulerian methods help to easily address the issues related to the mesh distortion, because the membrane is implicitly described. However, a good solver for the advection problem is usually required. In addition, several issues related to an excessive amount of mass loss or gain must be handled [39]. Among the existing methodologies, we can cite the volume-of-fluid method [40, 41], the phase field method [35, 42, 43], and the level set method [44–46]. In the present work, we use the level set method, where the cell membrane is implicitly described as a particular level set. Regarding the membrane incompressibility, it plays an essential role to get the observed shapes of RBCs, because it allows to preserve a fixed surface area. This constraint could be satisfied using a penalty approach [26, 46], or or by introducing a Lagrange multiplier [35]. The latter strategy is considered herein.

In what follows, we describe the model used to simulate the equilibrium shapes of RBCs. An Eulerian finite element method based on the level set approach is used. To overcome a usual drawback of Eulerian methods, we first employ a modified level set approach based on the imposition of additional constraints via some Lagrange multipliers that enable to enforce the mass conservation. Furthermore, a mesh adaptation technique is used to better capture the RBC membrane. A reduced order model helps to validate afterwards the computational results.

Outline. We have arranged the remainder of this paper as follows. In Section 2, we introduce the required notations, and we provide a consistent mathematical setting for the formulation of the physical model of minimal energy. A saddle point formulation allows us to characterize the solution in the weak formulation. We present a detailed description of the mixed finite element method, and we describe an anisotropic mesh adaptation procedure that helps to enhance the mass preservation. Section 3 outlines the detailed numerical algorithm. A set of numerical examples illustrating the main features of the model and the accuracy of the adaptive finite element computations are listed in Section 4. Some concluding remarks are provided in Section 5. Finally, a reduced order model describing the equilibrium of RBCs is derived in Appendix A and helps validate our computational results.

2. MATHEMATICAL MODEL FOR RBC's EQUILIBRIUM SHAPE

2.1. Notations

Let $\Lambda \subset \mathbb{R}^d, d \in \{2, 3\}$ be the bounded domain containing the RBC and the surrounding domain, where $L > 0$ represents the domain width. We assume that Λ is large enough so that the cell membrane never touch the boundary $\partial\Lambda$. Figure 1 provides a sketch of the cell membrane and the computational domain. Let $\boldsymbol{x}$ represent the spatial coordinate in the domain Λ at time t. Let us introduce the outward unit normal vectors $\mathbf{n}$ and $\boldsymbol{\nu}$, respectively, on Γ and $\partial\Lambda$ (Figure 1). Let $\Sigma_- = \{\boldsymbol{x} \in \partial\Lambda : \boldsymbol{u} \cdot \boldsymbol{\nu}(\boldsymbol{x}) < 0\}$ represent the upstream boundary. Let us consider a scalar function $\varkappa$ and a

DOI: 10.1002/fld

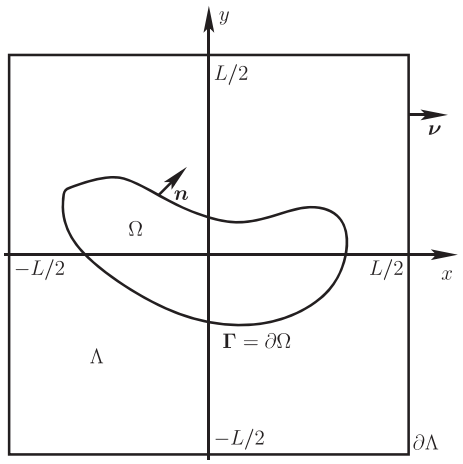

Figure 1. A sketch for the red blood cell embedded in the surrounding computational domain.

vector field $\boldsymbol{u}$. We define the tangential gradient, the tangential divergence, and the Laplace–Beltrami operator (called also surface Laplacian), which are given respectively by the following:

$$\begin{aligned} \nabla_s \varkappa &:= (\mathbf{I} - \mathbf{n} \otimes \mathbf{n})\, \nabla \varkappa = \nabla \varkappa - (\mathbf{n}.\nabla \varkappa)\, \mathbf{n} \\ \mathrm{div}_s(\mathbf{u}) &:= \mathrm{trace}(\nabla_s \varkappa) = (\mathbf{I} - \mathbf{n} \otimes \mathbf{n}) : \nabla \mathbf{u} \\ \Delta_s \varkappa &:= \mathrm{div}_s(\nabla_s \varkappa) \end{aligned} \tag{2.1}$$

where the symbol $\otimes$ denotes the tensorial product, and the semicolon (:) represents the two times contracted product between tensors.

2.2. *Level set formulation*

Let $T > 0$ and for any $t \in (0, T)$ let us assume that the domain within the cell has a smooth boundary $\Gamma = \partial\Omega$. We introduce a level set function φ defined in the domain Λ, in order to label the inside and the outside of the cell. The membrane Γ is given by the following:

$$\Gamma = \{(t, \boldsymbol{x}) \in (0, T) \times \Lambda : \varphi(t, \boldsymbol{x}) = 0\}. \tag{2.2}$$

It represents a particular level set of φ and, by convention, the set $\{(t, \boldsymbol{x}) \in (0, T) \times \Lambda : \varphi(t, \boldsymbol{x}) < 0\}$ represents the inner domain. The advection of the level set function enables to to follow the deformation of Γ, and we have

$$\partial_t \varphi + \boldsymbol{u} \cdot \nabla \varphi = 0 \ \text{ in } \ (0, T) \times \Lambda. \tag{2.3}$$

The advection field $\boldsymbol{u}$ will be obtained afterwards from a shape optimization problem (Section 2.4). Suitable initial and boundary conditions are required:

$$\varphi(0, \cdot) = \varphi_0(\cdot) \quad \text{in } \Lambda \qquad \text{and} \qquad \varphi = \varphi_b \quad \text{on } (0, T) \times \Sigma_-.$$

The function φ_0 acts as initial datum for (2.3), and it represents the `signed distance` to $\Gamma_0 = \partial\Omega_0$:

$$\varphi_0(\boldsymbol{x}) = \begin{cases} \inf\limits_{\boldsymbol{y} \in \Gamma_0} |\boldsymbol{y} - \boldsymbol{x}|, & \text{if } \boldsymbol{x} \notin \Omega_0, \\ -\inf\limits_{\boldsymbol{y} \in \Gamma_0} |\boldsymbol{y} - \boldsymbol{x}|, & \text{otherwise.} \end{cases}$$

DOI: 10.1002/fld

2.3. Redistancing and regularization

By solving the advection problem (2.3), the level set function φ loses its property of being a signed distance function, and $|\nabla\varphi| \neq 1 \in \Lambda$. We need to avoid this situation because too large or too small gradients of the level set function, notably around Γ and $\partial\Lambda$, indicate respectively either a steep or a flat function whose zero level set is less accurately tracked. An auxiliary problem called commonly the `redistancing problem` may be solved to recover the signed distance property. An accurate redistancing procedure should keep two properties: the inner volume Ω of the cell should be preserved and the zero-level set Γ should keep its initial position. To address these issues, we introduce a modified redistancing problem where a Lagrange multiplier located in the vicinity of Γ is introduced to enhance the local mass conservation [47]. Let $\tilde{\varphi}(t,.)$ be the solution of (2.3) at time $t \in (0,T)$. We introduce a pseudo-time variable τ. Initialized with $\tilde{\varphi}$, we consider the following Hamilton–Jacobi equation

$$\begin{aligned} \frac{\partial\varphi}{\partial\tau}(\tau,\boldsymbol{x};t) + \boldsymbol{v}\cdot\nabla\varphi(\tau,\boldsymbol{x};t) &= sgn\left(\tilde{\varphi}(t,\boldsymbol{x})\right) + \lambda(\tau,x;t)\, g\left(\varphi(\tau,\boldsymbol{x};t)\right) \quad \text{a.e. in } (0,+\infty)\times\Lambda, \\ \varphi(0,\boldsymbol{x};t) &= \tilde{\varphi}(t,\boldsymbol{x}) \qquad\qquad\qquad\qquad\qquad\qquad\quad \text{a.e. in } \Lambda. \end{aligned} \tag{2.4}$$

The advection vector writes $\boldsymbol{v} = sgn(\tilde{\varphi})\nabla\varphi/|\nabla\varphi|$, and $sgn\,(\tilde{\varphi})$ denotes the sign function having the values $0,-1,+1$ on Γ, inside Ω and outside Ω, respectively. The Lagrange multiplier $\lambda(\tau,\boldsymbol{x};t)$ helps enforce the constraint of a local constant volume at each $\boldsymbol{x}\in\Lambda$. The function $g(\varphi)$ localizes the mass correction in the vicinity of the interface, and it depends on the Dirac measure $\delta(\varphi)$. As a consequence, the stationary solution satisfies $|\nabla\varphi| = 1$ meaning that $\varphi(\infty,.;t)$ is a signed distance, which is taken as the new level set function $\varphi(t,.)$. More details about the numerical discretization of (2.4) are available in [14, 47]. For a given $\varepsilon > 0$, the Heaviside function, the sign function, and the Dirac measure are regularized in a banded region of width 2ε around Γ. They are respectively substituted by $\mathscr{H}_\varepsilon$, δ_ε, and sgn_ε. For all φ, they are, respectively, defined by

$$\mathscr{H}_\varepsilon(\varphi) = \begin{cases} 0, & \text{if } \varphi < -\varepsilon \\ \dfrac{1}{2}\left(1 + \dfrac{\varphi}{\varepsilon} + \dfrac{\sin\left(\frac{\pi\varphi}{\varepsilon}\right)}{\pi}\right), & \text{if } |\varphi| \leqslant \varepsilon \\ 1, & \text{otherwise} \end{cases}, \qquad \mathrm{sgn}_\varepsilon(\varphi) = 2\mathscr{H}_\varepsilon(\varphi) - 1\,,$$

$$\delta_\varepsilon(\varphi) = \frac{\mathrm{d}\mathscr{H}_\varepsilon}{\mathrm{d}\varphi}(\varphi) = \frac{1}{2\varepsilon}\left(1 + \cos\left(\frac{\pi\varphi}{\varepsilon}\right)\right) \quad \text{if } |\varphi| \leqslant \varepsilon, \quad \text{and} \quad 0 \text{ otherwise.}$$

2.4. Governing equations

In this section, we state the equations governing the model. The Canham and Helfrich energy reads as follows:

$$\mathcal{J}(\Omega) = \int_{\partial\Omega} \frac{k}{2}(H(\Omega) - H_0)^2\,\mathrm{d}s. \tag{2.5}$$

The RBC's membrane Γ is described by Equation (2.2), and the energy $\mathcal{J}(\Omega)$ has to be encoded in terms of φ. Let $\mathbb{V}$ denote the space of the admissible shapes. A shape optimization problem describes the equilibrium of RBCs:

$$\Omega = \arg\inf_{w\in\mathbb{V}} \mathcal{J}(w) \qquad \text{with } \mathbb{V} = \left\{\omega \subset \Lambda \,:\, \int_{\partial\omega} \mathrm{d}s = A_0 \text{ and } \int_\omega \mathrm{d}x = V_0\right\} \tag{2.6}$$

where A_0 and V_0 represent the surface area and the volume enclosed inside the cell, respectively, at time $t = 0$. In the two-dimensional case, A_0 and V_0 represent the perimeter and the inner area of the cell, respectively. Because the spontaneous curvature has no effect on the equilibrium shape in the

DOI: 10.1002/fld

two-dimensional case [25, 26, 48], we assume herein that $H_0 = 0$. The constrained problem (2.6) is transformed into a saddle point problem, and we introduce the Lagrangian functional:

$$\mathcal{L}(\omega;\sigma,q) = \mathcal{J}(\omega) + \sigma\left(\int_{\partial\omega} \mathrm{d}s - A_0\right) + q\left(\int_{\omega} \mathrm{d}x - V_0\right), \quad \forall(\omega;\sigma,q),$$

where σ and q represent the Lagrange multipliers corresponding respectively to the surface and the volume constraints. The solution $(\Omega; p, \lambda) \in (\Lambda; \mathbb{R}, \mathbb{R})$ is a saddle point of $\mathcal{L}$, and the problem writes

$$(\Omega;\lambda,p) = \underset{\omega\subset\Lambda}{\operatorname{arginf}} \sup_{\substack{\sigma\in\mathbb{R}\\ q\in\mathbb{R}}} \mathcal{L}(\omega;\sigma,q). \tag{2.7}$$

In order to solve (2.7), we use a gradient method, and we consider the notion of shape derivative introduced by [49]. We follow the approach developed by [50]. Let Ω represent a smooth reference domain describing the RBC. We consider a sufficiently regular shape deformation $\mathbf{u}$ such that the shape Ω is deformed to $\Omega_{\boldsymbol{u}} = (\mathbf{I}+\mathbf{u})(\Omega) = \{\mathbf{x}+\mathbf{u}(\mathbf{x}) \in \Lambda : \mathbf{x} \in \Omega\}$, where $\mathbf{I}$ represents the identity transformation. The shape derivative of $\mathcal{J}(\Omega)$ is defined as the Fréchet derivative at $\mathbf{0}$ of the application $\boldsymbol{u} \to \mathcal{J}((\mathbf{I}+\mathbf{u})(\Omega))$. Thereafter, we use the classical notation of the shape derivative in the direction $\mathbf{u}$, and the latter derivative is denoted $D'_{\Omega}\mathcal{J}(\Omega)(\boldsymbol{u})$, see, for example, [34, 50] for more details. Using the shape differentiation tools [32, 33, 43, 49, 50], we computed the Fréchet derivative of (2.6) in a previous work [34]. It reads

$$D'_{\omega}\mathcal{L}(\omega;\lambda,p)(\mathbf{u}) = \int_{\Gamma}\left\{p + \lambda H + \frac{1}{2}(H-H_0)[4K - H(H+H_0)] - \Delta_s H\right\}\mathbf{u}.\mathbf{n}\,\mathrm{d}s\,.$$

To minimize the Lagrangian $\mathcal{L}$, the descent direction is given by

$$\mathbf{u} = \left\{\Delta_s H - \frac{1}{2}(H-H_0)[4K - H(H+H_0)] - p - \lambda H\right\}\mathbf{n}.$$

Let t design the time parameter that corresponds to the descent stepping [50]. We update the shape as $\omega_{\boldsymbol{u}}(t) = (\mathbf{I}+t\mathbf{u})(\omega)$ and we obtain the following:

$$\mathcal{L}(\omega_{\boldsymbol{u}}(t);\lambda,p) = \mathcal{L}(\omega;\lambda,p) - \mathrm{t}\int_{\Gamma}\left\{\Delta_s H - \frac{1}{2}(H-H_0)[4K - H(H+H_0)] - p - \lambda H\right\}^2 \mathrm{ds} + \mathcal{O}(\mathrm{t}^2),$$

which ensures the decrease of the objective functional. The vector $\mathbf{u}$ represents the advection field, and it depends on the level set function φ and on the geometrical parameters H, K, and $\mathbf{n}$. These quantities are initially set on the membrane Γ. However, they should be encoded in terms of φ and then extended to the entire computational domain Λ. Equipped with suitable initial and boundary conditions, we obtain the following Hamilton–Jacobi problem:

$\mathcal{P}$: find φ, p , and λ such that

$$\frac{\partial\varphi}{\partial t} + \left[\Delta_s H - \frac{1}{2}(H-H_0)[4K - H(H+H_0)] - p - \lambda H\right]\mathbf{n}.\nabla\varphi = 0, \qquad \text{in } (0,T)\times\Lambda \tag{2.8a}$$

$$\int_{\Omega} \mathrm{d}x = V_0, \qquad \text{in } (0,T) \tag{2.8b}$$

$$\int_{\partial\Omega} \mathrm{d}s = A_0, \qquad \text{in } (0,T)$$
$$\varphi(0,\cdot) = \varphi_0(\cdot) \text{ in } \Lambda \qquad \text{and} \qquad \varphi = \varphi_b \text{ on } (0,T)\times\Sigma_-. \tag{2.8c}$$

DOI: 10.1002/fld

2.5. Variational formulation

We present in this section the variational formulation of (2.8a), (2.8b), and (2.8c). At each time t, we assume enough regularity of the shape Ω. To encode the vector of the gradient descent in terms of the level set φ, we prove that

$$H(H^2 - 4K) = 2H\nabla.\left(\frac{\nabla_s|\nabla\varphi|}{|\nabla\varphi|}\right) - \nabla.(H^2\mathbf{n}). \tag{2.9}$$

Indeed, by using the Einstein sum rule for repeated indices, we have

$$\begin{aligned}\nabla\mathbf{n} : \nabla\mathbf{n}^T &= \partial_j \boldsymbol{n}_i\, \partial_i \boldsymbol{n}_j = \partial_j\left(\boldsymbol{n}_i \partial_i \boldsymbol{n}_j\right) - \boldsymbol{n}_i \partial_i\left(\partial_j \boldsymbol{n}_j\right)\\ &= \nabla.\left[(\mathbf{n}\cdot\nabla)\,\mathbf{n}\right] - \mathbf{n}\cdot\nabla H = \nabla.\left((\mathbf{n}\cdot\nabla)\,\mathbf{n}\right) - \left(\nabla\cdot(H\mathbf{n}) - H^2\right).\end{aligned}$$

The Gauss curvature writes $2K = H^2 - \nabla\mathbf{n} : \nabla\mathbf{n}^T$, for example, [34]. We obtain

$$\begin{aligned}H(H^2 - 4K) &= H\left(-H^2 + 2\nabla\mathbf{n} : \nabla\mathbf{n}^T\right) = 2H\nabla\cdot\left((\mathbf{n}\cdot\nabla)\,\mathbf{n}\right) - H^3 - 2H\mathbf{n}\cdot\nabla H\\ &= 2H\nabla\cdot\left((\mathbf{n}\cdot\nabla)\,\mathbf{n}\right) - \nabla\cdot\left(H^2\mathbf{n}\right).\end{aligned}$$

Moreover, the equality $\partial_j|\nabla\varphi| = \partial_j\sqrt{\nabla\varphi.\nabla\varphi} = \dfrac{\partial_j\partial_k\varphi\ \partial_k\varphi}{|\nabla\varphi|}$ leads to

$$(\nabla\mathbf{n})_{ij} = \partial_j\left(\frac{\partial_i\varphi}{|\nabla\varphi|}\right) = \frac{|\nabla\varphi|\partial_j\partial_i\varphi\ -\ \partial_i\varphi\partial_j|\nabla\varphi|}{|\nabla\varphi|^2} = \frac{1}{|\nabla\varphi|}\left(\partial_j\partial_i\varphi\ -\ \frac{\partial_i\varphi}{|\nabla\varphi|}\,\frac{\partial_k\varphi}{|\nabla\varphi|}\,\partial_k\partial_j\varphi\right).$$

Then we get $|\nabla\varphi|\nabla\mathbf{n} = (\mathbf{I} - \mathbf{n}\otimes\mathbf{n})\cdot\nabla\nabla\varphi$. Because we have $\nabla(\nabla\varphi\cdot\nabla\varphi) = 2\,(\nabla\varphi\cdot\nabla)\,\nabla\varphi + 2\nabla\varphi\wedge\mathbf{rot}(\nabla\varphi) = 2\nabla(\nabla\varphi)\cdot\nabla\varphi$, we obtain $\nabla\nabla\varphi.\mathbf{n} = \dfrac{\nabla(\nabla\varphi)\cdot\nabla\varphi}{|\nabla\varphi|} = \dfrac{1}{2}\dfrac{\nabla\left(|\nabla\varphi|^2\right)}{|\nabla\varphi|} = \nabla|\nabla\varphi|$.

Accordingly, we obtain $(\mathbf{n}.\nabla)\mathbf{n} = \dfrac{1}{|\nabla\varphi|}\left((\mathbf{I} - \mathbf{n}\otimes\mathbf{n})\,.\nabla\nabla\varphi\right).\mathbf{n} = \dfrac{1}{|\nabla\varphi|}\,(\mathbf{I} - \mathbf{n}\otimes\mathbf{n})\,(\nabla\nabla\varphi.\mathbf{n}) = \dfrac{\nabla_s|\nabla\varphi|}{|\nabla\varphi|}$. Finally, Equation (2.9) holds. Let us consider a test function ξ. The variational formulation reads

$$\int_\Lambda \frac{\partial\varphi}{\partial t}\xi + \int_\Lambda \left[2\,\Delta_s H + H\,(H^2 - 4K)\right]|\nabla\varphi|\xi = 0, \qquad \forall\xi\in H_0^1(\Lambda). \tag{2.10}$$

Let φ_{min} and φ_{max} represent the maximal and minimal values of φ, respectively. By using the co-area formula, see for example [51], and the Green transformation, we obtain

$$\begin{aligned}\int_\Lambda |\nabla\varphi|\Delta_s H\,\xi\mathrm{dx} &= \int_{\varphi_{min}}^{\varphi_{max}}\int_{\varphi(x)=z}\Delta_s H\xi\,\mathrm{dsdz}\\ &= \int_{\varphi_{min}}^{\varphi_{max}}\left(-\int_{\varphi(x)=z}\nabla_s H\cdot\nabla_s\xi\,\mathrm{ds} + \int_{\varphi(x)=z}\xi H\underbrace{\mathbf{n}\cdot\nabla_s H}_{0}\,\mathrm{ds}\right)\mathrm{dz}\\ &= -\int_\Lambda |\nabla\varphi|\nabla_s H.\nabla_s\xi\,\mathrm{dx}.\end{aligned}$$

Because the surface projection operator verify $(\mathbf{I} - \mathbf{n}\otimes\mathbf{n})^2 = (\mathbf{I} - \mathbf{n}\otimes\mathbf{n})^T = (\mathbf{I} - \mathbf{n}\otimes\mathbf{n})$, we obtain $\displaystyle\int_\Lambda |\nabla\varphi|\Delta_s H\xi + \int_\Lambda |\nabla\varphi|\nabla_s H\cdot\nabla\xi = 0$. Using Equation (2.9), we obtain

DOI: 10.1002/fld

$$\int_\Lambda |\nabla\varphi| H(H^2-4K)\xi = 2\int_\Lambda |\nabla\varphi| H \nabla.\left(\frac{\nabla_s|\nabla\varphi|}{|\nabla\varphi|}\right)\xi - \int_\Lambda |\nabla\varphi|\nabla.(H^2\mathbf{n})\,\xi$$
$$= \int_\Lambda \left(H^2\nabla\varphi - 2H\nabla_s|\nabla\varphi|\right)\cdot\nabla\xi - 2\int_\Lambda \frac{\nabla|\nabla\varphi|}{|\nabla\varphi|}.\nabla_s\left(H|\nabla\varphi|\right)\xi$$
$$+ \int_\Lambda \frac{H^2}{|\nabla\varphi|}\nabla\varphi.\nabla(|\nabla\varphi|)\xi.$$

Using the equality $|\nabla\varphi|\nabla_s H + H\nabla_s|\nabla\varphi| = \nabla_s(|\nabla\varphi|H)$, Equation (2.10) reads

$$\int_\Lambda \frac{\partial\varphi}{\partial t}\xi - 2\int_\Lambda \nabla_s(H|\nabla\varphi|)\cdot\nabla\xi + \int_\Lambda H^2\nabla\varphi\cdot\nabla\xi$$
$$- 2\int_\Lambda \frac{\nabla|\nabla\varphi|}{|\nabla\varphi|}\cdot\nabla_s\left(H|\nabla\varphi|\right)\xi + \int_\Lambda \frac{H^2}{|\nabla\varphi|}\nabla\varphi\cdot\nabla(|\nabla\varphi|)\xi = 0.$$

To facilitate the numerical discretization, we write a mixed problem to decrease the derivation order of φ in the previous equation. Let us consider the mixed variable $\psi = -H|\nabla\varphi|$. For $(\xi,\zeta) \in H_0^1(\Lambda)\times H^1(\Lambda)$, we obtain the following:

$$\int_\Lambda \frac{\partial\varphi}{\partial t}\xi + \int_\Lambda \nabla_s\psi.\nabla\xi + \int_\Lambda \frac{\psi^2}{2|\nabla\varphi|^2}\nabla\varphi.\nabla\xi + \int_\Lambda \frac{\nabla|\nabla\varphi|}{|\nabla\varphi|}.\nabla_s\psi\xi$$
$$+ \int_\Lambda \frac{\psi^2}{2|\nabla\varphi|^3}\nabla\varphi.\nabla(|\nabla\varphi|)\xi - \int_\Lambda p|\nabla\varphi|\xi + \int_\Lambda \lambda\psi\xi = 0 \tag{2.11}$$

$$\int_\Lambda \frac{\psi}{|\nabla\varphi|}\zeta - \int_\Lambda \frac{1}{|\nabla\varphi|}\nabla\varphi.\nabla\zeta = 0. \tag{2.12}$$

From a numerical point of view, we give a particular attention to the skeleton of the level set function. In fact, the normal vector $\mathbf{n}$ becomes discontinuous when crossing this area, and a subdifferential of the level set function exists. In Figure 2, we show these particular areas in the cases of some elementary shapes. Observe that $|\nabla\varphi|$ has very small values, that is, around the machine precision. Therefore, the assembled matrix of the linear system of the discretized problem may become singular if some nodes are located in the skeleton. To address this difficulty, we decided to avoid the division by $|\nabla\varphi|$ in the weak formulation (2.11 and 2.12). Let us consider two integers $(k,l) \in \mathbb{N}^2$, and we introduce the test functions $(\tilde\xi,\tilde\zeta) \in H_0^1(\Lambda)\times H^1(\Lambda)$ such that $\xi = |\nabla\varphi|^l\tilde\xi$ and $\zeta = |\nabla\varphi|^k\tilde\zeta$. We obtain:

$$\int_\Lambda |\nabla\varphi|^l\partial_t\varphi\tilde\xi + \int_\Lambda |\nabla\varphi|^l\nabla_s(\psi)\cdot\nabla\tilde\xi + \frac{1}{2}\int_\Lambda |\nabla\varphi|^{l-2}\psi^2\nabla\varphi.\nabla\tilde\xi - \int_\Lambda p|\nabla\varphi|^{l+1}\tilde\xi$$
$$+\int_\Lambda (l+1)|\nabla\varphi|^{l-1}\nabla|\nabla\varphi|.\nabla_s(\psi)\tilde\xi + \frac{1}{2}\int_\Lambda (l+1)|\nabla\varphi|^{l-3}\psi^2\nabla\varphi\cdot\nabla(|\nabla\varphi|)\tilde\xi + \int_\Lambda \lambda\psi|\nabla\varphi|^l\tilde\xi = 0,$$
$$\int_\Lambda |\nabla\varphi|^{k-1}\psi\tilde\zeta - \int_\Lambda |\nabla\varphi|^{k-1}\nabla\varphi.\nabla\tilde\zeta = \int_\Lambda k|\nabla\varphi|^{k-2}\nabla\varphi\cdot\nabla|\nabla\varphi|\tilde\zeta.$$

By setting $l = 3$ and $k = 2$, we can avoid the division by $|\nabla\varphi|$. In what follows, we drop the tilde symbol to make it easier to read. Let us introduce the mixed variable γ given by

$$\gamma = \nabla|\nabla\varphi| \in \mathrm{H_0(div},\Lambda) := \left\{\boldsymbol{\tau} \in \left(L^2(\Lambda)\right)^d \,:\, \nabla\cdot\boldsymbol{\tau} \in L^2(\Lambda) \text{ and } \boldsymbol{\tau}\cdot\boldsymbol{\nu}_{\partial\Lambda} = 0 \text{ on } \partial\Lambda\right\}$$

Finally, the variational formulation reads as follows:
given φ_b and φ_0 regular enough; find $\mathbf{n}\in L^2\left((0,T);L^\infty(\Lambda)^d\right)$, $\gamma \in L^2\left((0,T);H_0(\mathrm{div},\Lambda)\right)$, $\psi \in L^2\left((0,T);H^1(\Lambda)\right)$, and $\varphi \in L^2\left((0,T);H_0^1(\Lambda)\cap W^{1,\infty}(\Lambda)\right)$ such that

DOI: 10.1002/fld

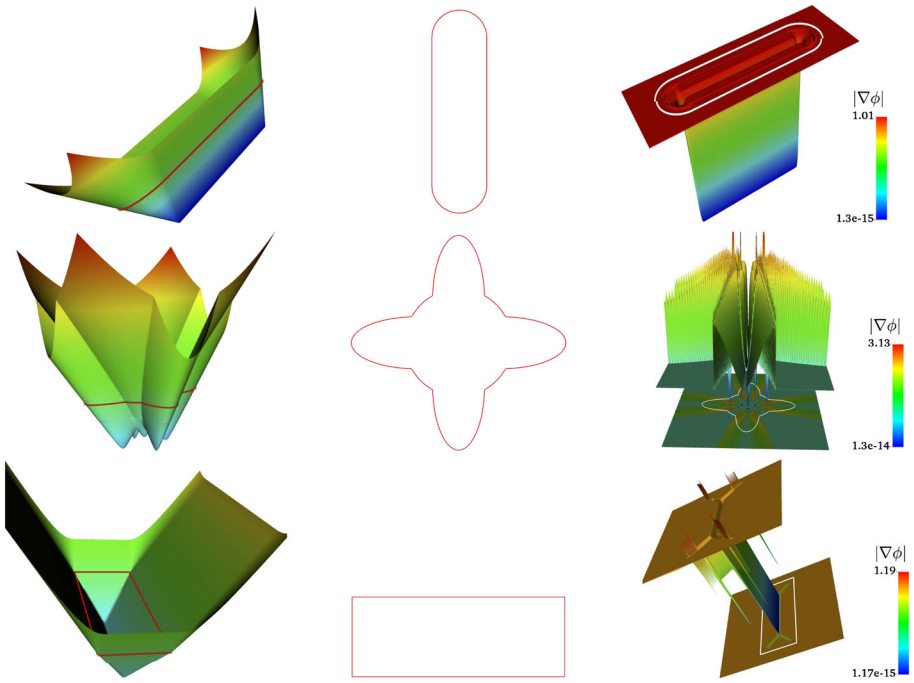

Figure 2. Singularity zone in the skeleton. (left) Level set φ plotted in elevation (zero-level set colored in red), (middle) zero-level set Γ, and (right) norm of the Ggadient $|\nabla\varphi|$ and its projection in the horizontal plan.

$$\int_\Lambda |\nabla\varphi|\mathbf{n}\cdot\varsigma = \int_\Lambda \nabla\varphi.\varsigma, \qquad \forall\varsigma \in \left(L^2(\Lambda)\right)^d \tag{2.13}$$

$$\int_\Lambda \gamma.\boldsymbol{\tau} = -\int_\Lambda |\nabla\varphi|\nabla\cdot\boldsymbol{\tau}, \qquad \forall\boldsymbol{\tau} \in H_0(\mathrm{div},\Lambda) \tag{2.14}$$

$$\int_\Lambda |\nabla\varphi|\psi\xi - \int_\Lambda |\nabla\varphi|\nabla\varphi.\nabla\xi = 2\int_\Lambda (\nabla\varphi\cdot\gamma)\xi, \qquad \forall\xi \in H^1(\Lambda) \tag{2.15}$$

$$\begin{aligned}&\int_\Lambda |\nabla\varphi|^3\nabla_s\psi.\nabla\zeta + \int_\Lambda |\nabla\varphi|^3\partial_t\varphi\zeta + \frac{1}{2}\int_\Lambda |\nabla\varphi|\psi^2\nabla\varphi\cdot\nabla\zeta\\ &-\int_\Lambda p|\nabla\varphi|^4\zeta + 4\int_\Lambda |\nabla\varphi|^2(\nabla_s\psi\cdot\gamma)\zeta + 2\int_\Lambda \psi^2(\nabla\varphi\cdot\gamma)\zeta + \int_\Lambda \lambda\psi|\nabla\varphi|^3\zeta = 0, \quad \forall\zeta \in \mathrm{H}_0^1(\Lambda).\end{aligned} \tag{2.16}$$

2.6. *Refinement and mesh adaptation technique*

Our approach bases on the work of the authors of [52, 53], and we use the bidirectional anisotropic mesh generator BAMG [54, 55]. We briefly describe the method, and we refer to [14, 56] for further details. Let us consider a field $\Xi(\varphi)$ suitably computed from the solution φ, and we introduce the metric tensor given by the Hessian matrix of Ξ [54]. The mesh is adapted to the computation of Ξ such that the interpolation error becomes uniformly distributed. It means the error becomes constant over all the mesh elements in the directions of maximal and minimal stretching, while the maximal and minimal directions of stretching have to be adjusted to the directions of maximal and minimal error. At each time t, we consider a partition $\mathscr{T}_h$ such that $\overline{\Lambda} = \bigcup_{K\in\mathscr{T}_h}$ (Section 3.3). Let the subscribes ξ and x stand for the reference and the deformed configurations, respectively.

DOI: 10.1002/fld

Let $X_K : \boldsymbol{\xi} \longmapsto \mathbf{x} = M_K\boldsymbol{\xi} + \mathbf{t}_K$ be the affine transformation that maps the reference triangle K_ξ into K_x as depicted in Figure 3, where M_K and $\mathbf{t}_K$ represent the Jacobian of the transformation X_K and a translation, respectively. Because the triangle K is not flat, the matrix M_K is asymmetric and invertible, and it admits a singular value decomposition (SVD), for example, [57–59]. The SVD expresses the matrix M_K as a product $M_K = R_K^T \Lambda_K P_K$, where R_K and P_K are orthogonal and Λ_K is a diagonal matrix with positive entries. Because the reference triangle K_ξ is equilateral, the transformed triangle K_x is inscribed in the ellipse $(\boldsymbol{x} - \mathbf{t}_K)^T R_K^T \Lambda_K^{-2} R_K (\boldsymbol{x} - \mathbf{t}_K) = 1$. Following [54, 55], the interpolation error is estimated by $h^2_{K,\mathbf{v}} |\mathbf{v}^T (\nabla\nabla\Xi)\mathbf{v}|$, where $h_{K,\mathbf{v}}$ represents the length of K in the direction $\mathbf{v}$. We use piecewise linear and continuous functions to approximate the field Ξ over each triangle $K \in \mathscr{T}_h$, while an L^2 projection enables then to compute the Hessian $\nabla\nabla\Xi$. Let $(\lambda_{x_1}, \lambda_{x_2})$ and $(\boldsymbol{v}_1, \boldsymbol{v}_2)$ design the eigenvalues and the eigenvectors of $\nabla\nabla\Xi$, respectively. The mesh adaptation consists in shrinking K in both directions $\boldsymbol{v}_1$ and $\boldsymbol{v}_2$. The directional sizes $h_{K,\mathbf{v}_1}$ and $h_{K,\mathbf{v}_2}$ are then adjusted such that the interpolation error becomes equidistributed. In the present work, we need to refine the mesh in the vicinity of the RBC membrane to accurately compute geometrical quantities like H, n, and the surface operators. Accordingly, we choose $\Xi = \sum_{i=n-1}^{n} \delta_\varepsilon(\varphi^i)$ at each time t^n. When big deformations are observed, we also add a second term that represents a prediction of the solution at time t^{n+1} (Section 4.2.3). Regarding the regularization parameter ε, we choose it proportional to the local value of the mesh size $\varepsilon(\boldsymbol{x}_i) = 2\sqrt{2\text{meas}(\text{C}_\text{i})}$, where C_i is the finite volume cell centered in $\boldsymbol{x}_i$; it joins the barycenters of the triangles and the middle points of edges passing through $\boldsymbol{x}_i$ (Figure 4).

Thus, the remeshing procedure can provide an adaptive mesh with high mesh density in the surrounding of the membrane. In general, the aspect ratio (i.e., stretching) of the mesh triangles can be arbitrarily large, depending on the local value of the Hessian of the criterion Ξ [56]. To evaluate the quality of the mesh elements, we define the aspect ratio of a triangle $K \in \mathscr{T}_h$ as the ratio between the longest edge length and the shortest edge length in K. In Figure 4 (middle), the mesh

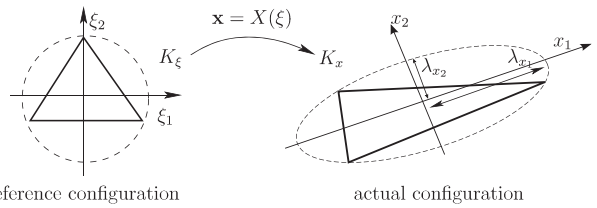

Figure 3. Transformation from the reference element K_ξ to the triangle K_x in the actual configuration.

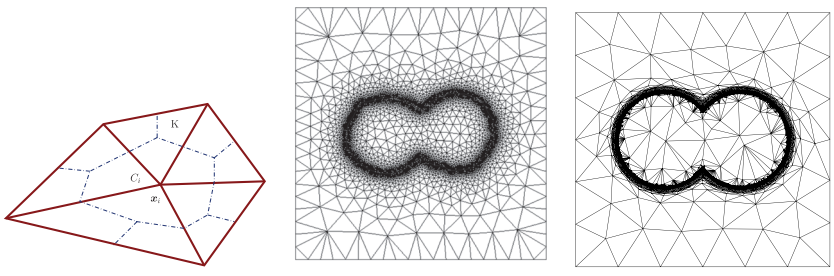

Figure 4. (left) Finite volume cell C_i centered in the vertex x_i. (middle) Adapted mesh in the vicinity of the RBC with 10 732 triangles and 5 407 vertices. (right) Adapted mesh in the vicinity of the RBC with 46 070 triangles and 23 048 vertices.

DOI: 10.1002/fld

quality is characterized by an aspect ratio in [1.01, 3.04] (isotropic adaptive), while the mesh has an aspect ratio in [1, 26.20] in Figure 4 (right) (anisotropic adaptive). We note that further improving the mesh anisotropy and the alignment with the RBC membrane represent an interesting topic that is definitely beyond the goal of this work.

3. NUMERICAL APPROXIMATION

3.1. Time discretization

To discretize the problem (2.13, 2.14, 2.15, and 2.16) in time, we divide the interval $[0, T]$ into N subintervals $[t_n, t_{n+1})$ of constant step Δt where $n = 0, \ldots, N-1$. For any $n \geqslant 1$, the unknowns ψ^n and φ^n at t^n are computed recursively. For a given function $\mathcal{F} \in \mathcal{C}^1([0, T])$ and $t \in (0, T)$, we choose a second order backward differentiation formula:

$$\mathcal{F}'(t) \approx \frac{3}{2}\frac{\mathcal{F}^{n+1} - \mathcal{F}^n}{\Delta t} \quad \text{if } n = 1 \qquad \text{and} \qquad \mathcal{F}'(t) \approx \frac{3\mathcal{F}^{n+1} - 4\mathcal{F}^n + \mathcal{F}^{n-1}}{2\Delta t} \quad \text{if } n > 1.$$

Hence, one can expect that the error follows the evolution $\mathcal{O}(h^k) + \mathcal{O}\left(\triangle t^2\right)$ where k represents the degree of the finite element discretization in space. The theoretical analysis regarding the error estimation is preserved for a forthcoming work. We introduce the weighted multi-linear forms

$$m(w, \xi, \zeta) = \int_\Lambda w\, \xi\zeta \qquad \text{for all } w \in L^\infty(\Lambda), \xi \in L^2(\Lambda) \text{ and } \zeta \in L^2(\Lambda)$$

$$a(\mathbf{T}, \xi, \zeta) = \int_\Lambda (\mathbf{T}\nabla\xi) \cdot \nabla\zeta \qquad \text{for all } \mathbf{T} \in (L^\infty(\Lambda))^{d\times d}, \xi \in H^1(\Lambda) \text{ and } \zeta \in H^1(\Lambda).$$

A semi-implicite scheme is used for the time discretization of (2.15) and (2.16). We obtain

$\mathcal{P}_t$: given $\varphi^n_{\partial\Lambda} \in H^1(\Lambda) \cap W^{1,\infty}(\Lambda)$, $\varphi^0_0 = \varphi_0^{-1} \in L^2(\Lambda)$, $\mathbf{n}^n \in L^\infty(\Lambda)^d$, $\boldsymbol{\gamma}^n \in H_0(\mathrm{div}, \Lambda) \cap L^\infty(\Lambda)^d$ and $(p^n, \lambda^n) \in \mathbb{R}^2$;

find $\psi^{n+1} \in H^1(\Lambda) \cap L^\infty(\Lambda)$ and φ^{n+1} with $\varphi^{n+1} - \varphi^n_{\partial\Lambda} \in H^1_0(\Lambda) \cap W^{1,\infty}(\Lambda)$ such that

$$m\left(|\nabla\varphi^n|, \psi^{n+1}, \xi\right) - a\left(|\nabla\varphi^n|\mathbf{I}, \varphi^{n+1}, \xi\right) = 2m\left(\nabla\varphi^n.\boldsymbol{\gamma}^n, 1, \xi\right)$$

$$a\left(|\nabla\varphi^n|^3(\mathbf{I} - \mathbf{n}^n \otimes \mathbf{n}^n), \psi^{n+1}, \zeta\right) + \frac{3}{2\triangle t}m\left(|\nabla\varphi^n|^3, \varphi^{n+1}, \zeta\right) + \frac{1}{2}a\left(|\nabla\varphi^n|\,(\psi^n)^2\,\mathbf{I}, \varphi^{n+1}, \zeta\right) =$$

$$\frac{1}{2\triangle t}m\left(|\nabla\varphi^n|^3\left(4\varphi^n - \varphi^{n-1}\right), 1, \zeta\right) - m\left(\lambda^n\psi^n|\nabla\varphi^n|^3, 1, \zeta\right) \tag{3.1a}$$

$$- m\left(4|\nabla\varphi^n|^2\,(\mathbf{I} - \mathbf{n}^n \otimes \mathbf{n}^n)\,\nabla\psi^n.\boldsymbol{\gamma}^n + 2(\psi^n)^2\,(\nabla\varphi^n \cdot \boldsymbol{\gamma}^n) - p^n|\nabla\varphi^n|^4, 1, \zeta\right) \tag{3.1b}$$

for all $\xi \in H^1(\Lambda)$ and $\forall\zeta \in H^1_0(\Lambda)$.

3.2. Algorithm for the saddle point problem

To compute the saddle points of the Lagrangian $\mathcal{L}(\Omega; p, \lambda)$, we use an Uzawa-type algorithm [60–63]. This algorithm performs in two steps: it first minimizes the Lagrangian with respect to the shape, and then the Lagrange multipliers are computed by minimizing the dual energy $\mathscr{E}^*(p, \lambda)$ (Algorithm 1). The small step length δ helps to perform the descent in the direction opposite to the gradient of $\mathscr{E}^*(p, \lambda)$. The stopping criterion should be given by the residual. At each t^n, we compute the two residuals res^n_{II} and res^n_I of Equations (3.1a) and (3.1b), respectively. We define the global residual by $|\mathrm{res}^n| = \sqrt{|\mathrm{res}^n_I|^2 + |\mathrm{res}^n_{II}|^2}$, where $|\cdot|$ denotes an appropriate norm (Section 3.3). Remark that, by using a constant descent step δ, the Uzawa algorithm only preserves the constraints in the convergence. However, they can be verified if the Uzawa algorithm is used with an optimal descent step at each iteration. The Uzawa algorithm with the exact descent step is shown in Algorithm 2.

DOI: 10.1002/fld

Algorithm 1 Uzawa with a fixed descent step δ

set tolerance ϵ and initial conditions Ω^0, p^0, and λ^0
from the known values Ω^n, p^n, and λ^n
for $t = n\Delta t, \cdots, T$ **do**
  compute $\Omega^{n+1} \subset \Lambda$ such that $\mathcal{L}(\Omega^{n+1}; p^n, \lambda^n) < \mathcal{L}(\Omega^n; p^n, \lambda^n)$
  set $\mathscr{E}^*(p, \lambda) := -\mathcal{L}(\Omega^{n+1}; p, \lambda)$ and compute $\left(p^{n+1}, \lambda^{n+1}\right) = (p^n, \lambda^n) - \delta \nabla_{p,\lambda} \mathscr{E}^* (p^n, \lambda^n)$
  compute residual $|\mathrm{res}^{n+1}|$
  if $|\mathrm{res}^{n+1}| < \epsilon$ **then**
    break
  end if
end for

Algorithm 2 Uzawa with optimal descent step

set tolerance ϵ and initial conditions
from known values Ω^n, p^n, and λ^n
for $t = n\Delta t, \cdots, T$ **do**
  compute $\Omega^{n+1} \subset \Lambda$ such that $\mathcal{L}(\Omega^{n+1}; p^n, \lambda^n) < \mathcal{L}(\Omega^n; p^n, \lambda^n)$
  compute $\left(p^{n+1}, \lambda^{n+1}\right) = (p^*, \lambda^*)$ such that $V = V_0$ and $A = A_0$
  compute $|\mathrm{res}^{n+1}|$
  if $|\mathrm{res}^{n+1}| < \epsilon$ **then**
    break
  end if
end for

Computation of the optimal Lagrange multipliers. In this section, we proceed to compute the exact values of the Lagrange multipliers p^* and λ^*. Using (2.9), the problem $\mathcal{P}$ (2.8a, 2.8b, and 2.8c) writes

$$\frac{\partial \varphi}{\partial t} + \left[\Delta_s H + H\nabla.\left[\frac{\nabla_s|\nabla\varphi|}{|\nabla\varphi|}\right] - \frac{1}{2}\nabla.\left(H^2\mathbf{n}\right) - p - \lambda H\right]|\nabla\varphi| = 0 \qquad \text{in } (0,T)\times\Lambda \quad (3.2)$$

$$\frac{d}{dt}\int_\Lambda \mathscr{H}(\varphi) = 0 \qquad \text{in } (0,T) \quad (3.3)$$

$$\frac{d}{dt}\int_\Gamma 1 = 0 \qquad \text{in } (0,T). \quad (3.4)$$

By using the Reynolds formula, Equation (3.4) is equivalent to

$$\int_\Gamma \nabla_s.\mathbf{u} = 0 \Leftrightarrow \int_\Gamma H\mathbf{u}\cdot\mathbf{n} = 0 \Leftrightarrow p\int_\Gamma H + \lambda\int_{\partial\Omega} H^2$$
$$= \int_\Gamma H\Delta_s H + \int_\Gamma H^2\nabla\cdot\left(\frac{\nabla_s|\nabla\varphi|}{|\nabla\varphi|}\right) - \frac{1}{2}\int_\Gamma H\nabla\cdot\left(H^2\mathbf{n}\right).$$

In addition, Equation (3.3) is equivalent to

$$\int_\Lambda \frac{\partial\varphi}{\partial t}\delta(\varphi) = 0 \Leftrightarrow \int_\Gamma \frac{\partial\varphi}{\partial t}\frac{1}{|\nabla\varphi|} = 0 \Leftrightarrow p\int_\Gamma 1 + \lambda\int_{\partial\Omega} H$$
$$= \int_\Gamma \Delta_s H + \int_\Gamma H\nabla.\left[\frac{\nabla_s|\nabla\varphi|}{|\nabla\varphi|}\right] - \frac{1}{2}\int_\Gamma \nabla.\left(H^2\mathbf{n}\right).$$

DOI: 10.1002/fld

By using the Green's formula involving surface integrals and knowing that $\mathbf{n}.\nabla_s H = 0$, we have $\int_\Gamma \Delta_s H = \int_\Gamma H\mathbf{n}.\nabla_s H = 0$ and $\int_\Gamma H\Delta_s H = -\int_\Gamma |\nabla_s H|^2$. Hence, we obtain the system:

$$\begin{cases} p\int_\Gamma H + \lambda\int_\Gamma H^2 = -\int_\Gamma |\nabla_s H|^2 + \int_\Gamma H^2\nabla.\left[\frac{\nabla_s|\nabla\varphi|}{|\nabla\varphi|}\right] - \frac{1}{2}\int_\Gamma H\nabla.\left(H^2\mathbf{n}\right) \\ p\int_\Gamma 1 + \lambda\int_\Gamma H = \int_\Gamma H\nabla.\left[\frac{\nabla_s|\nabla\varphi|}{|\nabla\varphi|}\right] - \frac{1}{2}\int_\Gamma \nabla.\left(H^2\mathbf{n}\right). \end{cases}$$

Finally, the optimal Lagrange multipliers p^* and λ^* read as follows:

$$\begin{cases} \lambda^* = \dfrac{\int_\Gamma 1\times\int_\Gamma H^2\nabla\cdot\left(\frac{\nabla_s|\nabla\varphi|}{|\nabla\varphi|}\right) - |\nabla_s H|^2 - \frac{H}{2}\nabla\cdot\left(H^2\mathbf{n}\right)}{\int_\Gamma 1\int_\Gamma H^2 - \left(\int_\Gamma H\right)^2} - \dfrac{\int_\Gamma H\times\int_\Gamma H\nabla\cdot\left(\frac{\nabla_s|\nabla\varphi|}{|\nabla\varphi|}\right) - \frac{\nabla\cdot\left(H^2\mathbf{n}\right)}{2}}{\int_\Gamma 1\int_\Gamma H^2 - \left(\int_\Gamma H\right)^2} \\ p^* = \dfrac{\int_\Gamma H\nabla.\left(\frac{\nabla_s|\nabla\varphi|}{|\nabla\varphi|}\right) - \frac{1}{2}\int_\Gamma \nabla.\left(H^2\mathbf{n}\right) - \lambda\int_\Gamma H}{\int_\Gamma 1}. \end{cases} \tag{3.5}$$

Equation (3.5) is simpler if φ is a signed distance where $\int_\Gamma H\nabla.\left(\frac{\nabla_s|\nabla\varphi|}{|\nabla\varphi|}\right) = \int_\Gamma H^2\nabla.\left(\frac{\nabla_s|\nabla\varphi|}{|\nabla\varphi|}\right) = 0$. However, we assume the membrane Γ never touch the skeleton of the function φ. Therefore, $|\nabla\varphi|$ is only evaluated in the vicinity of Γ where, thanks to the redistancing step, the level set is close to the signed distance. Consequently, the division by $|\nabla\varphi|$ in Equation (3.5) does not induce numerical singularities.

3.3. Space discretization by finite elements

We proceed with the space discretization of the problem $\mathcal{P}_t$ (3.1a and 3.1b). We consider a partition $\mathcal{T}_h$ of Λ consisting of geometrically conforming open simplicial elements K such that $\bar{\Lambda} = \cup_{K\in\mathcal{T}_h}$. Let $h = \max_{K\in\mathcal{T}_h} diam(K)$ be the mesh size if the mesh is regular. If the mesh is adapted, we compute the equivalent space discretization step $h_{eq} = 1/\sqrt{N_n}$, where N_n represents the number of nodes in the adapted mesh. A piecewise continuous finite element approximation is considered for the discretization of both φ and ψ. Let φ_h^n and ψ_h^n be the spatial approximation of φ^n and ψ^n, respectively, at the time step t^n. We introduce the following finite-dimensional spaces:

$$\mathbb{H}_h = \left\{\zeta_h \in \mathcal{C}^0\left(\overline{\Lambda}\right) : \zeta_{h|K} \in P_1(K), \forall K \in \mathcal{T}_h\right\}, \qquad \mathbb{G}_h = \mathbb{N}_h \cap H_0(\mathrm{div}, \Lambda),$$

$$\mathbb{N}_h = \mathbb{H}_h^d, \qquad \mathbb{V}_h(\xi_0) = \mathbb{H}_h \cap H_0^1(\Lambda) + \pi_h\left(\widetilde{\xi_0}\right),$$

where π_h represents a P_1 Lagrange interpolant on $\partial\Lambda$. Given $\xi_0 \in H^{1/2}(\partial\Lambda)$, the harmonic relevant $\widetilde{\xi_0}$ in the space $H^1(\Lambda)$ satisfies the following problem

$$\triangle\widetilde{\xi_0} = 0 \text{ in } \Lambda \qquad \text{such that} \qquad \widetilde{\xi_0} = \xi_0 \text{ on } \partial\Lambda.$$

Discretization of Equation (2.13). Let us consider $\varphi_h^n \in \mathbb{V}_h(\varphi_{\partial\Lambda})$, and we proceed to compute $\mathbf{n}_h^n \in \mathbb{N}_h$. The level set gradient vector $\nabla\varphi_h^n \in (P_0)^d$, $\forall K \in \mathcal{T}_h$. Let us denote by $\boldsymbol{g}_h^n$ by L^2 projection of $\nabla\varphi_h^n$ in $\mathbb{N}_h$, and we have

$$\int_\Lambda \boldsymbol{g}_h^n \cdot \varsigma_h = \int_\Lambda \nabla\varphi_h^n \cdot \varsigma_h, \quad \forall \varsigma_h \in \mathbb{N}_h. \tag{3.6}$$

DOI: 10.1002/fld

To assemble the left hand side of Equation (3.6), we use the lumped mass matrix, and the numerical computation of $\boldsymbol{g}_h^n$ is straightforward. Accordingly, the numerical approximation of the unit normal vector is given by

$$\mathbf{n}_h^n(x_i) = \begin{cases} \frac{\boldsymbol{g}_h^n(x_i)}{|\boldsymbol{g}_h^n(x_i)|} & \text{if } \left|\boldsymbol{g}_h^n(x_i)\right| \neq 0 \\ \mathbf{0} & \text{otherwise.} \end{cases} \tag{3.7}$$

Discretization of Equation (2.14). We consider an explicit scheme for the numerical approximation of $\boldsymbol{\gamma}^n$. Given the discretized level set function $\varphi_h^n \in \mathbb{V}_h(\varphi_{\partial\Lambda})$, the problem reads find $\boldsymbol{\gamma}_h^n \in \mathbb{G}_h$ such that for all $\boldsymbol{\tau} \in \mathbb{G}_h$, we have

$$\int_\Lambda \boldsymbol{\gamma}_h^n.\boldsymbol{\tau} + \int_\Lambda \left|\nabla\varphi_h^n\right| \nabla\cdot\boldsymbol{\tau} = 0. \tag{3.8}$$

Finally, with an exact evaluation of the multi-linear forms, the discrete problem $\mathcal{P}_t$ (3.1a and 3.1b) reads

$$\begin{aligned}
&\mathcal{P}_{t,h}^\star: \text{ given } \varphi_h^n \in \mathbb{V}_h(\varphi_0), \psi_h^n \in \mathbb{H}_h, \mathbf{n}_h^n \in \mathbb{N}_h \text{ and } \boldsymbol{\gamma}_h^n \in \mathbb{G}_h,\\
&\text{find } \left(\varphi_h^{n+1}, \psi_h^{n+1}\right) \in \mathbb{V}_h(\varphi_0)\times\mathbb{H}_h, \text{ such that } \forall(\zeta,\xi) \in \mathbb{V}_h(0)\times\mathbb{H}_h, \text{ we have}\\
&m\left(\left|\nabla\varphi_h^n\right|, \psi_h^{n+1}, \xi\right) - a\left(\left|\nabla\varphi_h^n\right|\mathbf{I}, \varphi_h^{n+1}, \xi\right) = 2m\left(\nabla\varphi_h^n.\boldsymbol{\gamma}_h^n, 1, \xi\right),\\
&a\left(\left|\nabla\varphi_h^n\right|^3\left(\mathbf{I}-\mathbf{n}_h^n\otimes\mathbf{n}_h^n\right), \psi_h^{n+1}, \zeta\right) + m\left(\frac{3\left|\nabla\varphi_h^n\right|^3}{2\Delta t}, \varphi_h^{n+1}, \zeta\right)\\
&+ a\left(\frac{\left|\nabla\varphi_h^n\right|}{2}\left(\psi_h^n\right)^2\mathbf{I}, \varphi_h^{n+1}, \zeta\right) = m\left(\frac{\left|\nabla\varphi_h^n\right|^3}{2\Delta t}\left(4\varphi_h^n - \varphi_h^{n-1}\right), 1, \zeta\right)\\
&-m\Big(4\left|\nabla\varphi_h^n\right|^2\left(\mathbf{I}-\mathbf{n}_h^n\otimes\mathbf{n}_h^n\right)\nabla\psi_h^n.\boldsymbol{\gamma}_h^n + 2\left(\psi_h^n\right)^2\left(\nabla\varphi_h^n.\boldsymbol{\gamma}_h^n\right) - p^n\left|\nabla\varphi_h^n\right|^4 + \lambda^n\psi_h^n\left|\nabla\varphi_h^n\right|^3, 1, \zeta\Big).
\end{aligned}$$

Using the finite element environment Rheolef [64], the exact evaluation of the multi-linear forms in $\mathcal{P}_{t,h}^\star$ is not feasible. However, the P_1 Lagrange interpolant π_h is used to approximate the weights in the previous forms, and the approximated problem reads as follows:

$$\begin{aligned}
&\mathcal{P}_{t,h}: \text{ given } \varphi_h^n \in \mathbb{V}_h(\varphi_0), \psi_h^n \in \mathbb{H}_h, \mathbf{n}_h^n \in \mathbb{N}_h \text{ and } \boldsymbol{\gamma}_h^n \in \mathbb{G}_h,\\
&\text{find } \left(\varphi_h^{n+1}, \psi_h^{n+1}\right) \in \mathbb{V}_h(\varphi_0)\times\mathbb{H}_h, \text{ such that } \forall(\zeta,\xi) \in \mathbb{V}_h(0)\times\mathbb{H}_h, \text{ we have}\\
&m\left(\pi_h\left[\left|\nabla\varphi_h^n\right|\right], \psi_h^{n+1}, \xi\right) - a\left(\pi_h\left[\left|\nabla\varphi_h^n\right|\mathbf{I}\right], \varphi_h^{n+1}, \xi\right) = 2m\left(\pi_h\left[\nabla\varphi_h^n.\boldsymbol{\gamma}_h^n\right], 1, \xi\right), \qquad (3.9)\\
&a\left(\pi_h\left[\left|\nabla\varphi_h^n\right|^3\left(\mathbf{I}-\mathbf{n}_h^n\otimes\mathbf{n}_h^n\right)\right], \psi_h^{n+1}, \zeta\right) + \frac{3}{2\triangle t}m\left(\pi_h\left[\left|\nabla\varphi_h^n\right|^3\right], \varphi_h^{n+1}, \zeta\right) +\\
&\frac{1}{2}a\left(\pi_h\left[\left|\nabla\varphi_h^n\right|\left(\psi_h^n\right)^2\mathbf{I}\right], \varphi_h^{n+1}, \zeta\right) = \frac{1}{2\triangle t}m\left(\pi_h\left[\left|\nabla\varphi_h^n\right|^3\left(4\varphi_h^n - \varphi_h^{n-1}\right)\right], 1, \zeta\right) -\\
&m\left(\pi_h\left[4\left|\nabla\varphi_h^n\right|^2\left(\mathbf{I}-\mathbf{n}_h^n\otimes\mathbf{n}_h^n\right)\nabla\psi_h^n\cdot\boldsymbol{\gamma}_h^n + 2\left(\psi_h^n\right)^2\left(\nabla\varphi_h^n\cdot\boldsymbol{\gamma}_h^n\right) - p^n\left|\nabla\varphi_h^n\right|^4 + \lambda^n\psi_h^n\left|\nabla\varphi_h^n\right|^3\right], 1, \zeta\right). \qquad (3.10)
\end{aligned}$$

Numerical computation of the residuals. The previous finite-dimensional linear system $\mathcal{P}_{t,h}$ involves the following matrix structure:

$$\begin{pmatrix} A_h^n & B_h^n \\ C_h^n & D_h^n \end{pmatrix} \cdot \begin{pmatrix} \Psi_h^{n+1} \\ \Phi_h^{n+1} \end{pmatrix} = \begin{pmatrix} F_h^n \\ G_h^n \end{pmatrix}$$

In the present work, this system is solved using the LU factorization of matrices performed by the UMFPACK library. Because the weighted bilinear forms depend on $\left(\Psi_h^n, \Phi_h^n\right)^T$ at the previous time step, the linear system needs to be assembled at each time step. The RBC problem $\mathcal{P}_{t,h}$ (3.9 and

DOI: 10.1002/fld

3.10) has a stationary solution, and the convergence criterion is based on the computation of the residual. Let us first consider Equation (3.1b) that includes the time derivative term. We denote by $\mathrm{res}^n_{I,h}$ the residual evaluated with the discrete H^{-1} norm at time t^n. For all $\zeta_h \in \mathbb{V}_h(0)$, the residual is given by

$$\mathrm{res}^n_{I,h}.\zeta^T_h = \left(\mathcal{A}^n_h \psi^n_h + \mathcal{B}^n_h \varphi^n_h - \mathcal{F}^n_h\right).\zeta^T_h,$$

where $\mathcal{A}^n_h$, $\mathcal{B}^n_h$, and $\mathcal{F}^n_h$ are the discrete operators corresponding to the forms in (3.10). The problem admits a stationary solution, and the residual verifies $\lim_{n\to\infty} \mathrm{res}^n_{I,h} = 0$. For all $\zeta_h \in \mathbb{V}_h(0)$, the discrete norm of the residual, simply denoted $|\cdot|_{\mathrm{H}_\mathrm{h}^{-1}}$, is defined by duality such that

$$\left|\mathrm{res}^n_{I,h}\right|_{\mathrm{H}_\mathrm{h}^{-1}} = \sup_{\zeta_h \in \mathbb{V}_h(0)} \frac{< \zeta_h, \mathrm{res}^n_{I,h} >_{\mathbb{V}_h(0),\mathrm{H}_\mathrm{h}^{-1}}}{|v_h|_{\mathbb{V}_h(0)}} = \sup_{\substack{v_h \in \mathbb{V}_h(0):\\ |v_h|_{\mathbb{V}_h(0)} = 1}} < v_h, \mathrm{res}^n_{I,h} >_{\mathbb{V}_h(0),\mathrm{H}_\mathrm{h}^{-1}}$$

$$= \max_{i \leqslant \dim(\mathbb{V}_h(0))} < \overline{\phi_{i,h}}, \mathrm{res}^n_{I,h} >_{\mathbb{V}_h(0),\mathrm{H}_\mathrm{h}^{-1}} = \max_{x \in \#\mathrm{dof}(\mathbb{V}_h(0))} \left|\mathrm{res}^n_{I,h}(x)\right|,$$

where $\overline{\phi_{j,h}}$ represents the normalized nodal finite element basis of $\mathbb{V}_h(0)$. The integer $\dim(\mathbb{V}_h(0))$ represents the dimension of $\mathbb{V}_h(0)$, and $\#\mathrm{dof}(\mathbb{V}_h(0))$ denotes the set of nodes associated to the degrees of freedom of $\mathbb{V}_h(0)$. Analogously, the norm of the discrete residual $\mathrm{res}^n_{II,h}$ corresponding (3.9) computed.

3.4. Numerical verification of the volume and area constraints

Let us consider a RBC having reduced area $\gamma = 0.75$, and we solve the problem $\mathcal{P}_{t,h}$ (3.10) following Algorithm 2. We plot in Figure 5 the evolution of the energy of Canham and Helfrich and the relative error in area and perimeter. Although the energy $\mathcal{J}$ is decreasing, results show that the constraints of area and perimeter are not verified and an error is accumulated significantly over the iterations. Remark that these errors are expected, because the constraints (2.8b) and (2.8c) are respectively replaced by (3.3) and (3.4) to allow the computation of the Lagrange multipliers. However, the two equations are equivalent up to a constant value that could represent the numerical errors because of the rounding and the interpolations between spaces. Thereafter, we need to substitute these errors by adding the appropriate corrections when computing the optimal Lagrange multipliers p^* and λ^*. The corresponding analytical computations will be provided in the following paragraph.

A posteriori correction of the Lagrange multipliers. To overcome the mass preservation problems, we introduce two parameters ε^n_V and ε^n_A needed for the error corrections in (3.3) and (3.4),

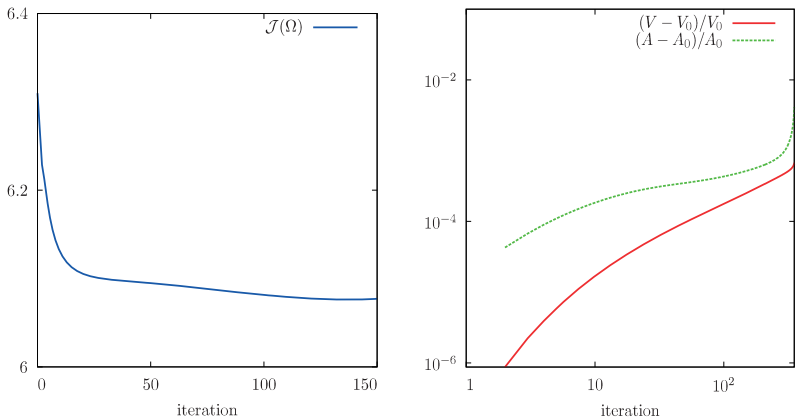

Figure 5. Preservation of the volume and the area. (left) Evolution of the energy of Canham and Helfrich and (right) plot in the logarithmic scale of the relative errors with respect to the iterations.

DOI: 10.1002/fld

respectively. At time t^n, we have $\varepsilon_A^n = \dfrac{A_0 - \int_{\Gamma^n} 1 \mathrm{ds}}{\Delta t}$ and $\varepsilon_V^n = \dfrac{\int_{\Omega^n} 1 \mathrm{dx} - V_0}{\Delta t}$. Therefore, $\mathcal{P}$ (2.8a, 2.8b, and 2.8c) is replaced by the following:

$$\begin{aligned}
&\frac{\partial \varphi}{\partial t} + \left[\Delta_s H - H\nabla.\left(\frac{\nabla_s|\nabla\varphi|}{|\nabla\varphi|}\right) - \frac{1}{2}\nabla\cdot\left(H^2\mathbf{n}\right) - p - \lambda H\right]|\nabla\varphi| = 0 \qquad \text{in } (0,T)\times\Lambda,\\
&\frac{d}{dt}\int_\Lambda \mathscr{H}(\varphi) = \varepsilon_V^n \qquad \text{in } (0,T),\\
&\frac{d}{dt}\int_\Gamma 1 = \varepsilon_A^n \qquad \text{in } (0,T).
\end{aligned}$$

By following the steps performed in Section 3.2, the corrected Lagrange multipliers read as follows:

$$\begin{cases}
\lambda = \lambda^* + \delta\lambda^n \qquad \text{with} \qquad \delta\lambda^n = \dfrac{-\varepsilon_A^n \int_\Gamma 1 - \varepsilon_V^n \int_\Gamma H}{\int_\Gamma 1 \int_\Gamma H^2 - \left(\int_\Gamma H\right)^2}\\[2ex]
p = p^* + \delta p^n \qquad \text{with} \qquad \delta p^n = \dfrac{\varepsilon_A^n \int_\Gamma 1 \int_\Gamma H + \varepsilon_V^n \int_\Gamma 1 \int_\Gamma H^2}{\int_\Gamma 1 \left(\int_\Gamma 1 \int_\Gamma H^2 - \left(\int_\Gamma H\right)^2\right)}.
\end{cases} \tag{3.11}$$

Remark that the corrections of the Lagrange multipiers can be interpreted as a *posteriori* control on the values of λ^* and p^* (3.5). Thus, the a posteriori corrections $\delta\lambda^n$ and δp^n of the Lagrange multipliers vanish if the errors ε_V^n and ε_A^n are null. The modified algorithm used to solve the saddle point problem is detailed in Algorithm 3, and we illustrate a full description of the numerical strategy in Figure 6.

Algorithm 3 Uzawa with *a posteriori* control

```
set tolerance ϵ
set initial conditions (Ω^0; p^0, λ^0)
from the known values Ω^n, p^n, and λ^n
for t = nΔt, ··· , T do
    compute Ω^{n+1} such that
    L(Ω^{n+1}; p^n, λ^n) ⩽ L(Ω^n; p^n, λ^n)
    compute (p^{n+1}, λ^{n+1}) (3.11)
    compute |res_h^{n+1}|_{H_h^{-1}}
    if |res_h^{n+1}|_{H_h^{-1}} < ϵ then
        break
    end if
end for
```

4. NUMERICAL SIMULATIONS

4.1. Software implementation

The presented method has been implemented using the Rheolef environment[‡] [64], which is a general purpose C++ library for scientific computing, with special emphasis on finite elements and

[‡]Rheolef - http://www-ljk.imag.fr/membres/Pierre.Saramito/rheolef/.

DOI: 10.1002/fld

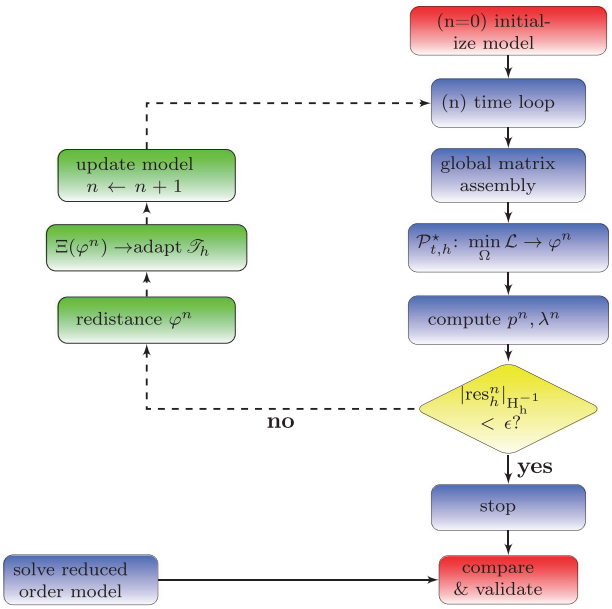

Figure 6. Illustration of the numerical methodology.

parallel computation. Rheolef provides support for distributed-memory parallelism via MPI[§]. Rheolef relies upon the Boost[¶], Blas[‖], and UMFPACK[**] libraries for much of its functionality. Rheolef bases on Scotch for distributed mesh partitioning[††]. The reduced order problem has been numerically solved with the free software package GNU Octave [65][‡‡]. The computational results are displayed graphically using the software Paraview[§§], whereas the plots are generated using the software Gnuplot[¶¶].

4.2. *Validation of the numerical solver*

We present in this section a set of numerical examples illustrating the main features and the accuracy of the numerical method. We first focus on our mesh adapting tool.

4.2.1. Example 1: the test of Zalesak's rigid disk. We first study the motion of a rigid body under the effect of a prescribed rotational motion. This test has been initially proposed by Zalesak [66]. It has become one of the most common test for interface propagation used to test numerical methods, for example, [67]. We are interested in the rotation of a slotted circle with a radius of 1/5, a slot depth of 3/10, and a width of 1/10. The slotted circle is initially centered at $(0.5, 7/10)$, and we consider a rotational velocity field given by $u = \left(\frac{\pi}{314}(50-y), \frac{\pi}{314}\cos(x-50)\right)^T$. The computational domain is the square $[0,1]^2$, and the slotted circle completes one revolution after one period. Several mesh sizes were considered to check the mesh dependency, and the convergence properties of our method. We plot in Figure 7 the convergence of the error between the computed solution φ_h and the exact solution φ with respect to the equivalent space discretization $h_{eq} = 1/\sqrt{N_n}$, where N_n represents the number of nodes in the adapted mesh (Section 3.3). The error is plotted in the logarithmic scale, and results show that we obtain better convergence slope first by adding the mass correction

[§]Message passing interface - http://www.mpich.org.
[¶]Boost libraries - http://www.boost.org.
[‖]BLAS, Basic Linear Algebra Subprograms library - http://www.netlib.org/blas.
[**]UMFPACK routines - http://www.cise.ufl.edu/research/sparse/umfpack/.
[††]Scotch - http://www.labri.fr/perso/pelegrin/scotch.
[‡‡]Octave - www.gnu.org/software/octave/.
[§§]Paraview - http://www.paraview.org
[¶¶]Gnuplot - http://www.gnuplot.info.

DOI: 10.1002/fld

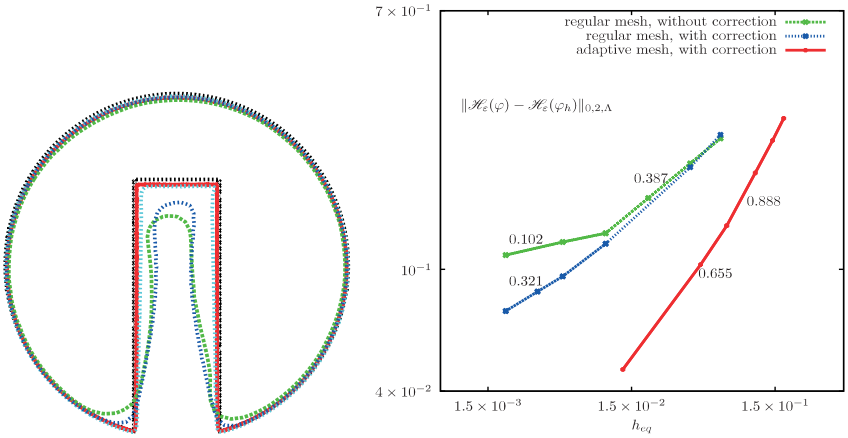

Figure 7. Example 1: (left) contour plots of the rotating slotted circle after one rotating period: exact solution (black and dotted), regular mesh without mass correction (green and dashed), regular mesh with mass correction (blue and dotted line), and adaptive mesh with mass correction (red and solid line) and (right) convergence properties in log-log scale.

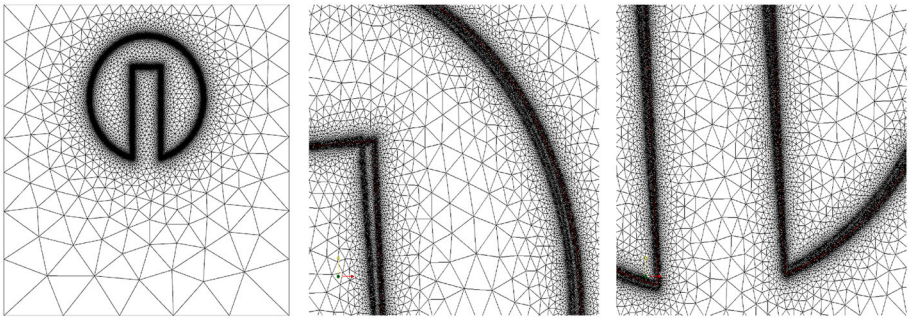

Figure 8. Example 1: adapted mesh in the Zalesak's test.

in the redistancing problem and second by using the mesh adaptation technique. Regarding the mesh adaptation, we consider the hessian matrix of the field $\Xi_h^n = \delta_\varepsilon\left(\varphi_h^n\right) + \delta_\varepsilon\left(\varphi_h^{n-1}\right)$. Figure 8 shows the accuracy of our meshing tool, in particular concerning the capture of the corners in the slotted disk.

4.2.2. Example 2: the test of Leveque's deformable disk. We study the advection of a deformable object in a shear flow field. This problem is used to test the ability of the numerical method to resolve and maintain thin filaments. This allows to capture, subsequently, some particular biconcave shapes of RBCs. This test was proposed by Leveque [68], and it is widely used to test numerical methods and strategies [69]. The computational domain is $\Lambda = [0,1]^2$. We consider an initial deformable circle having a radius 0.15 and centered in $(0.35, 0.35)$. The circle is advected in a vortex with a periodic velocity field given by $\mathbf{u}(x,y) = \left(2(sin(\pi x))^2 sin(2\pi y) sin(\pi t), -(sin(\pi y))^2 sin(\pi t) sin(2\pi x)\right)^T$. It reaches the maximum of deformation at the middle of the time period. The velocity components change then their signs, and the deformable circle again reaches its original position at the end of the period. This test shows the ability of our mesh technique to detect the thin filaments, as depicted in Figure 9.

4.2.3. Example 3: mean curvature motion. We study the mean curvature motion. We are interested in the time evolution of $\Gamma_0 = \partial\Omega_0$ such that, at each time $t \in (0,T)$, the curve $\Gamma(t) = \partial\Omega(t)$ moves with a normal speed given by the mean curvature. The advection vector is given by $u = -\mathrm{H}n$. This is a shape optimization problem that consists in minimizing the perimeter:

DOI: 10.1002/fld

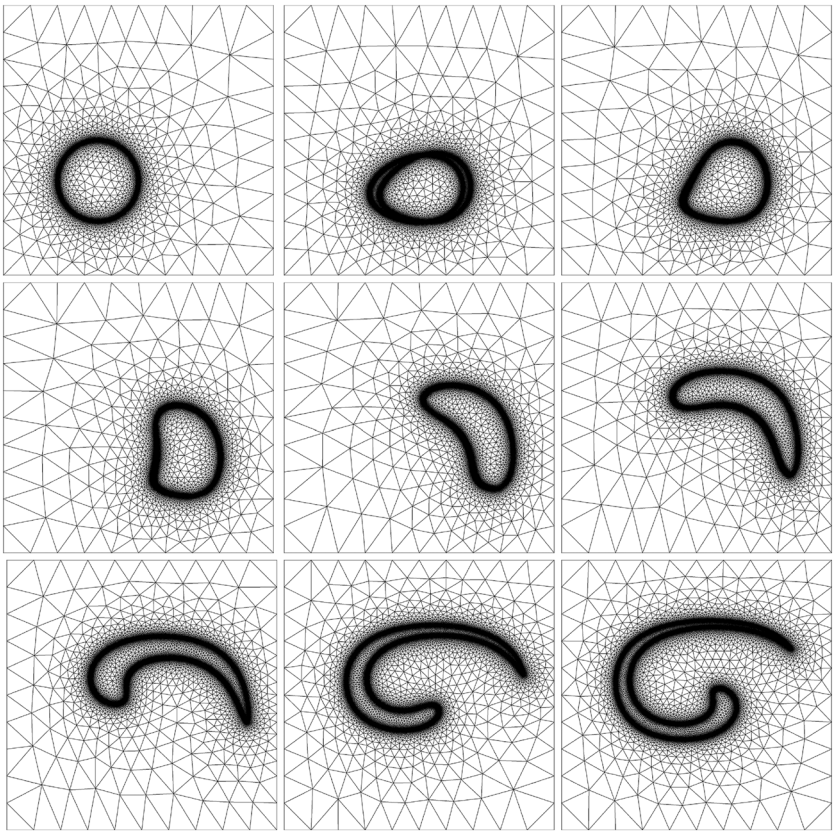

Figure 9. Example 2: some adaptive meshes obtained in the test of Leveque's deformable circle.

$$\Omega = \arg\min_{w} \int_{\partial w} 1 \, \mathrm{ds}.$$

The shape of a circle following the motion by mean curvature is well known. The initial circle remains a circle and shrinks into a point in a finite time. We solve this problem to test the mesh adaptation technique for a problem which also evolves the mean curvature. In fact, the mean curvature is a quantity that plays a significant role in the modelization of RBCs, and we need to compute it in an accurate way. To adapt the mesh, we choose the metric as the hessian of the field $\Xi_h^n = \delta_\varepsilon\left(\varphi_h^n\right) + \delta_\varepsilon\left(\varphi_h^{n+0.5}\right) + \delta_\varepsilon\left(\varphi_h^{n-1}\right)$ where $\varphi_h^{n+0.5}$ represents a first approximation of the solution at t^{n+1}, that is, a prediction, computed using the previous mesh generated using the criterion Ξ_h^{n-1}. Figure 10 shows the adapted meshes obtained using the previous criterion. We plot in Figure 11 the convergence of the error between the computed solution φ_h and the exact solution φ with respect to the equivalent space discretization h_{eq}. The error is plotted in the logarithmic scale, and results show that the convergence slope is improved by the mesh adaptation.

4.3. Numerical results in the two-dimensional case

In this section, we provide some numerical results of the equilibrium shapes of RBCs in the two-dimensional case. Because we do not dispose of an analytical expression describing the RBC's shape in the equilibrium state, a validation of the adaptive finite element method can be obtained by solving the reduced order problem (A.8). By varying the reduced area of the cell, we compare between the results obtained by the finite element solver and the results of the reduced order model as illustrated in Figure 6. Concerning the numerical computations in the two-dimensional case, through a re-scaling step, we may provide shapes having a fixed perimeter A_0 and variable surface area. In all the results, we consider the RBC's perimeter at time $t = 0$ to be 2π. We give a particular attention to the preservation of the area and the perimeter of the RBC, because it represents an important numerical

DOI: 10.1002/fld

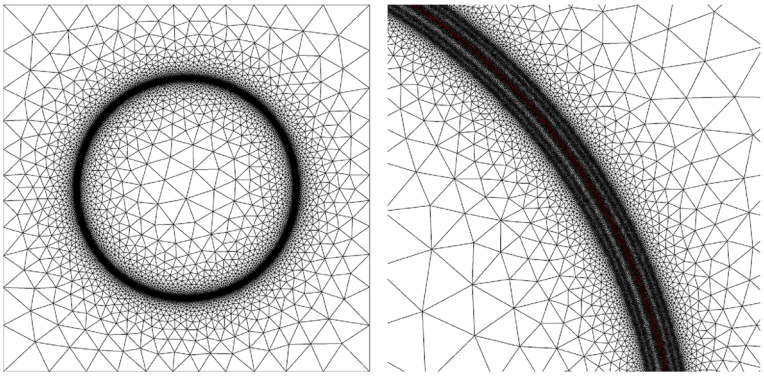

Figure 10. Example 3: (left) adaptive mesh and zoom showing the effect of using the adaptive criterion.

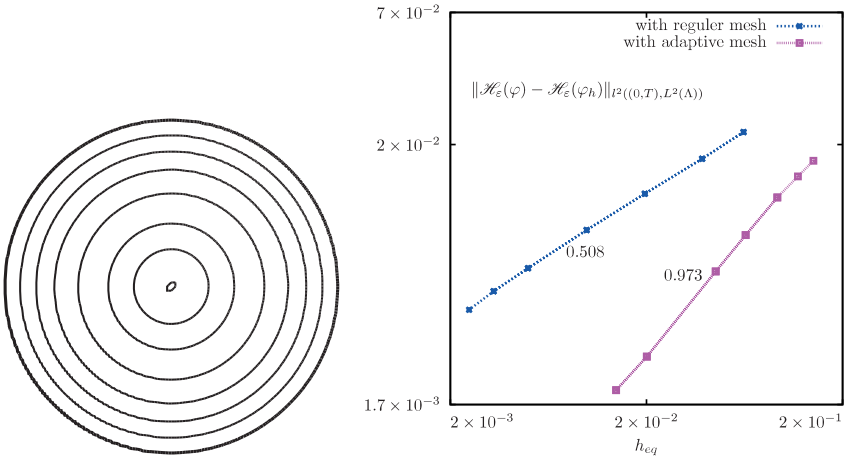

Figure 11. Example 3: (left) evolution of a circle that shrinks into a point in a finite time and (right) convergence properties in the $l^2((0,T);L^2(\Lambda))$ norm. The logarithmic scale is used.

difficulty related to the Eulerian methods. We first consider the numerical simulation of a biconcave RBC having a reduced area $\gamma = 0.75$. Concerning the convergence to the steady state describing the RBC's equilibrium, Figure 12 (right) depicts the convergence history showing the discrete H^{-1} norm of the residual res_h^n as described in Section 3.3. Results show that the residual reaches a plateau that should decrease with respect to Δt. In a similar way, we plot in Figure 13 the convergence history of the relative errors in the L^2 norm and the residual evaluated using the L^1 and L^2 norms for various values of the time step. An element that deserves more attention is the preservation of the perimeter and the area enclosed inside the cell. For a particular numerical computation, the quality of the numerical result and the preservation of the constraints are affected by the choice of time step Δt. Our concern here is to test the preservation of the constraints of perimeter and area for different time step sizes. In this numerical experiment, we focus on the equilibrium of the same RBC having a reduced area $\gamma = 0.75$ starting from the same initial shape and using different time step sizes, see Figure 14 (left) for an illustration of the equilibrium configuration of the cell. We plot in Figure 15(left) and Figure 15(right) the evolution of the relative error in the area and the perimeter. Numerical results show that errors are preserved remarkably well, and they are smaller than $10^{-5}\%$ when the time step size is smaller than 10^{-7}. We verify also that the convergence is obtained for the two Lagrange multipliers p and λ. Figure 12(left) shows their plots for a RBC having $\gamma = 0.75$ and using a time step size $\Delta t = 5 \times 10^{-9}$. The different simulations are all stopped when the residual $\left|\text{res}_h^n\right|_{\text{H}_\text{h}^{-1}}$ reaches the tolerance criterion $\epsilon = 10^{-5}$. The numerical results Pconfirm, as expected, that the Lagrange multipliers converge to the constant values $p = 3.3$ and $\lambda = -0.95$ in the steady state. In the following, the time step is set equal to $\Delta t = 5 \times 10^{-7}$. We

DOI: 10.1002/fld

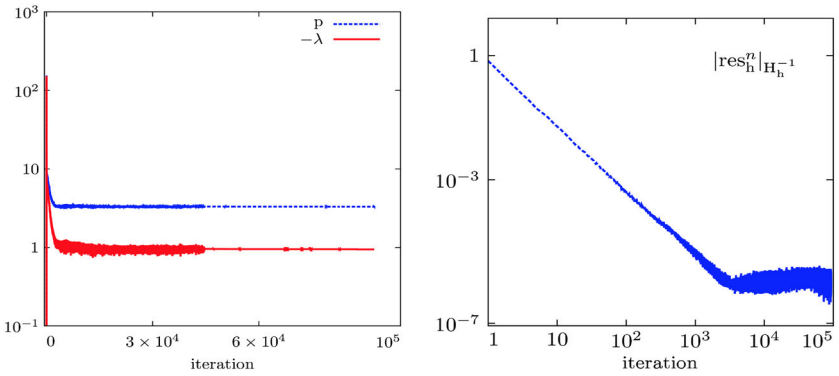

Figure 12. (left) Evolution of the Lagrange multipliers. The y-coordinate is scaled logarithmically and (right) convergence in the logarithmic scale of the residual with respect to the iteration number.

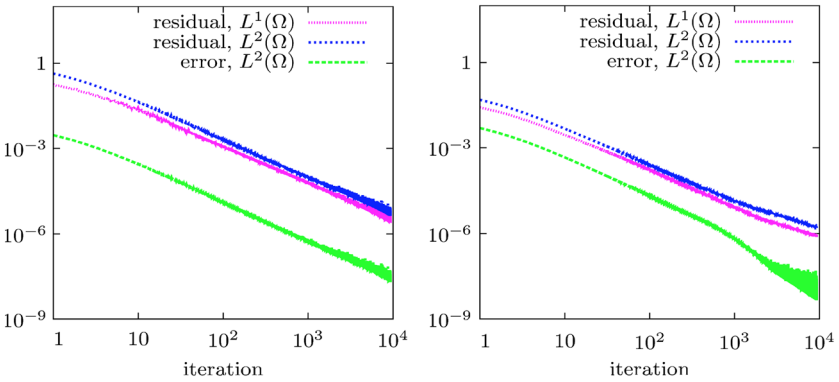

Figure 13. Convergence in several norms of the residual and the error using two different time step sizes: (left) $\Delta t = 10^{-8}$ and (right) $\Delta t = 10^{-7}$. Results are plotted in the logarithmic scale.

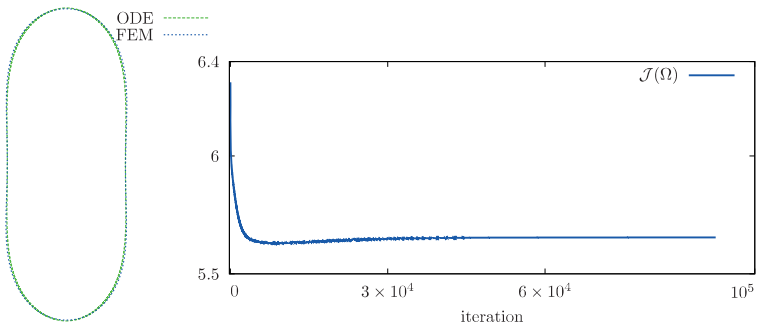

Figure 14. Equilibrium shape of a red blood cell having $\gamma = 0.75$: (left) comparison between the finite element solution (FEM) and the solution given by the reduced model (ODE) and (right) minimization of the Canham–Helfrich energy.

perform a qualitative comparison with the results obtained by solving the reduced order model (A.8). Regarding the numerical resolution of (A.8), we assume that the grid is uniform, and we consider the spatial discretization parameter $N = 10^4$ that corresponds to a mesh grid size $\Delta x = x_f/N$. The solution of the ordinary differential Equation A.9 having the same reduced area $\gamma = 0.75$ as the RBC is obtained by setting the parameters $\lambda = -0.95$, $p = 3.3$, and $w'(0) = 0.296$. A satisfactory agreement is observed with respect to the finite element solution in Figure 14(left). Figure 14(right) plots the evolution of the Canham–Helfrich energy with respect to the iterations. The tracing shows that the energy is decreasing before getting a stationary constant value equal to 5.68.

DOI: 10.1002/fld

We now present some other computational results that illustrate various shapes of RBCs and the corresponding reduced areas and energies of Canham and Helfrich. This experiment given in Figure 16 is designed to validate the equilibrium shape of a cell having a reduced area $\gamma = 0.85$. The finite element results shows that the energy of Canham and Helfrich is decreasing with respect to the iterations, and the corresponding final energy value is 4.64, as depicted in Figure 16(right). The solution of the reduced model having the same reduced area $\gamma = 0.85$ is obtained by using the following parameters: $N = 10^4, \lambda = -0.95$, $p = 3.3$, and $w'(0) = 0.48$. The two equilibrium shapes are almost the same, as shown in Figure 16(left).

The next experiment concerns the equilibrium shape of a cell having a reduced area $\gamma = 0.65$. The solution of the reduced model having the same reduced area is obtained by solving the ordinary differential Equation (A.8) using the parameters $N = 10^4, \lambda = -0.9$, $p = 3.2$, and $w'(0) = 0.296$.

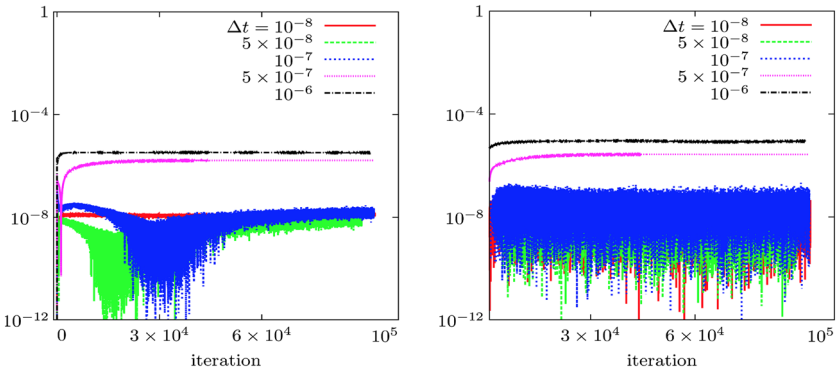

Figure 15. Evolution of the relative errors for different values of Δt. The y-coordinate is scaled logarithmically. (left) Relative error of the area and (right) relative error of the perimeter.

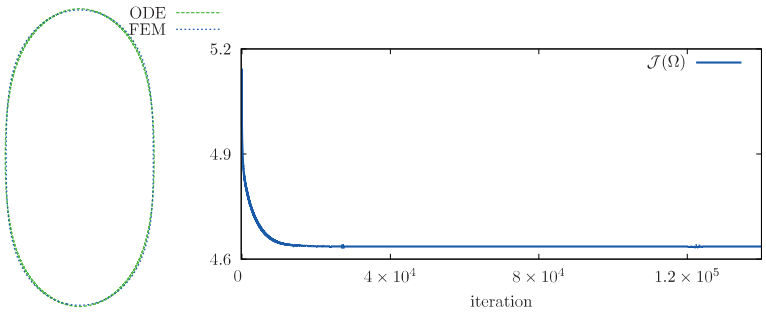

Figure 16. Evolution to the equilibrium shape of a red blood cell having $\gamma = 0.85$: (left) comparison between the FEM and the ODE solutions and (right) minimization of the Canham–Helfrich energy.

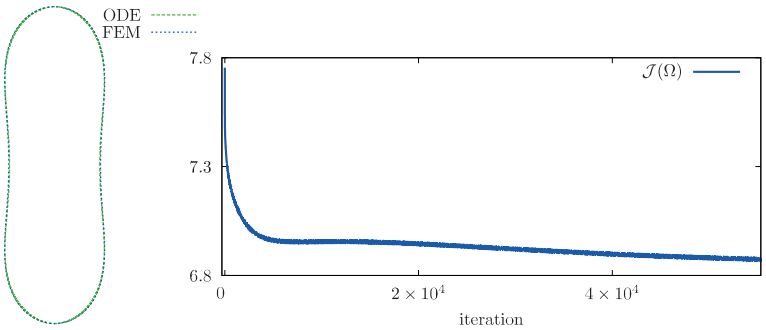

Figure 17. Evolution to the equilibrium shape of a red blood cell having $\gamma = 0.85$: (left) comparison between the FEM and the ODE solutions and (right) minimization of the Canham-Helfrich energy.

DOI: 10.1002/fld

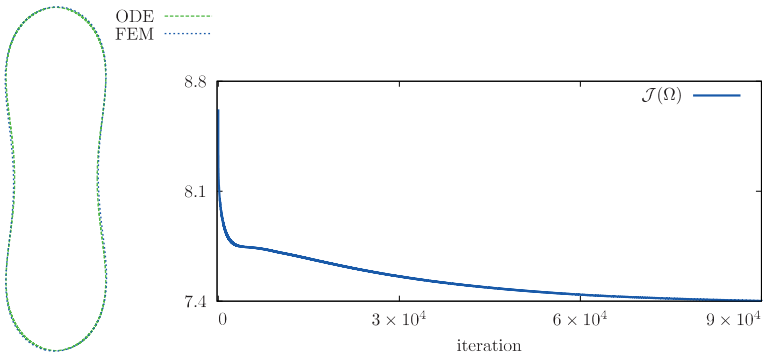

Figure 18. Evolution to the equilibrium shape of a red blood cell having $\gamma = 0.60$: (left) comparison between the FEM and the ODE solutions and (right) minimization of the Canham–Helfrich energy.

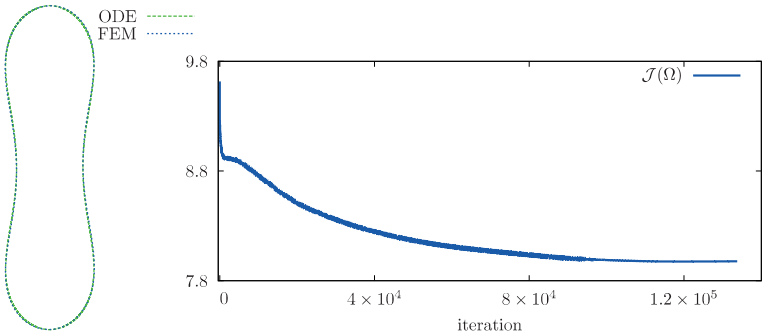

Figure 19. Evolution to the equilibrium shape of a red blood cell having $\gamma = 0.55$: (left) comparison between the FEM and the ODE solutions and (right) minimization of the Canham–Helfrich energy.

We solve the finite element problem, and results illustrated in Figure 17(left) show that both forms are almost the same. The corresponding energy of Canham and Helfrich decreases to a constant value, and the final energy value is around 6.89.

We consider in the next numerical test a cell with the reduced area $\gamma = 0.6$. For the same reduced area, the solution obtained by solving the reduced order problem is obtained using the parameters $N = 10^4, \lambda = -0.9, p = 3.2$, and $w'(0) = 0.4$. A satisfactory agreement is observed with respect to the finite element solution in Figure 18(left). Figure 18(right) plots the minimization of the energy of Canham and Helfrich with respect to the iterations. The energy is decreasing before getting a stationary constant value around 7.4.

The next numerical test considers a RBC having a reduced area $\gamma = 0.55$. The solution having the same reduced area obtained by solving the ordinary differential Equation (A.8) is obtained by setting $N = 10^4, \lambda = -0.95, p = 3.3$, and $w'(0) = 0.48$. By comparing with the results of the finite element solver, we clearly notice the similarities between the two forms, as shown in Figure 19(left). The evolution of the energy is plotted in Figure 19(right). Observe that the constant final value is equal to 8.04.

In the final simulation, we provide a numerical validation of the equilibrium shape of a RBC having a reduced area $\gamma = 0.49$. We obtain the solution of the reduced order model having the same shape parameter γ by using the following numerical parameters $N = 10^4, \lambda = 0, p = 3.3$, and $w'(0) = 0.55$. In Figure 20(left), we overlay this solution with the shape obtained by the finite element computations. The similarity between the two shapes is observed. We show in Figure 20(right) that the energy of Canham and Helfrich converges to a constant value equal to 9.2.

To summarize, the aforementioned numerical simulations in the two-dimensional case illustrate the robustness of the finite element solver modeling the static equilibrium of RBCs with the model introduced by Canham and Helfrich. The validation step is performed by comparing the finite

DOI: 10.1002/fld

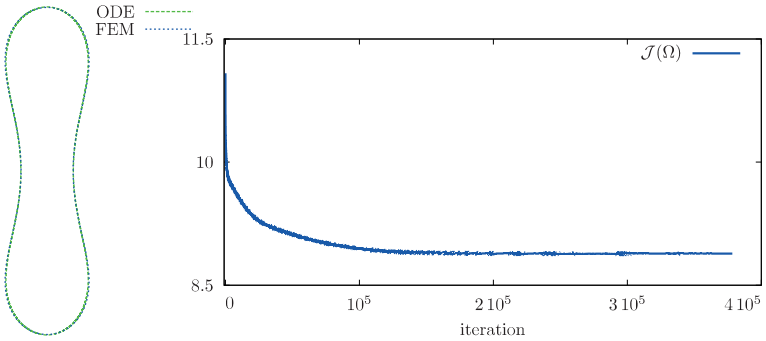

Figure 20. Evolution to the equilibrium shape of a red blood cell having $\gamma = 0.49$: (left) comparison between the FEM and the ODE solutions and (right) minimization of the Canham–Helfrich energy.

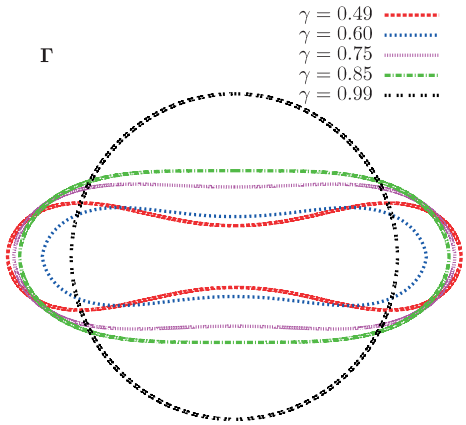

Figure 21. Two-dimensional case: overlay of some equilibrium shapes Γ of red blood cells with respect to their reduced areas. A dimensionless representation with a constant perimeter $A_0 = 2\pi$ is considered.

$\|\mathscr{H}_\varepsilon(\varphi_{\mathrm{ODE}}) - \mathscr{H}_\varepsilon(\varphi_{\mathrm{h}})\|_{0,2,\Lambda}$			
h_{eq}	$\gamma = 0.75$	$\gamma = 0.85$	$\gamma = 0.95$
0.052	0.03	0.027	0.015
0.036	0.0085	0.0077	0.005
0.017	0.0020	0.0018	0.00086
0.011	0.00102	0.0008	0.00044
0.006	0.0004	0.00022	0.000102

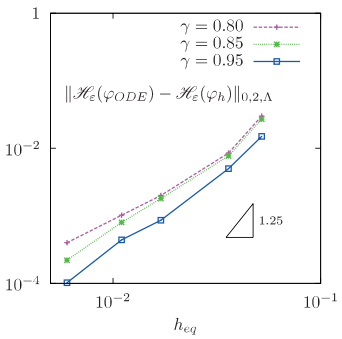

Figure 22. Convergence properties of the numerical method: evolution of the error, computed in the $L^2(\Lambda)$ norm, with respect to the equivalent mesh size h_{eq} for several values of the reduced area γ.

element computations with the results of the reduced order model. Furthermore, we superpose in Figure 21 some equilibrium shapes of RBCs having different reduced areas γ. These shapes are given by the finite element computations.

Convergence properties of the numerical method. In this paragraph, we investigate numerically the convergence properties of prescribed finite element solution. The spatial accuracy is studied by computing the error in the L^2 norm on successively refined meshes with respect to the reference solution obtained by solving the reduced order problem. The comparison is performed for three different RBCs having, respectively, the reduced area $\gamma \in \{0.80, 0.85 \text{ and } 0.95\}$. Table 22(left) depicts

DOI: 10.1002/fld

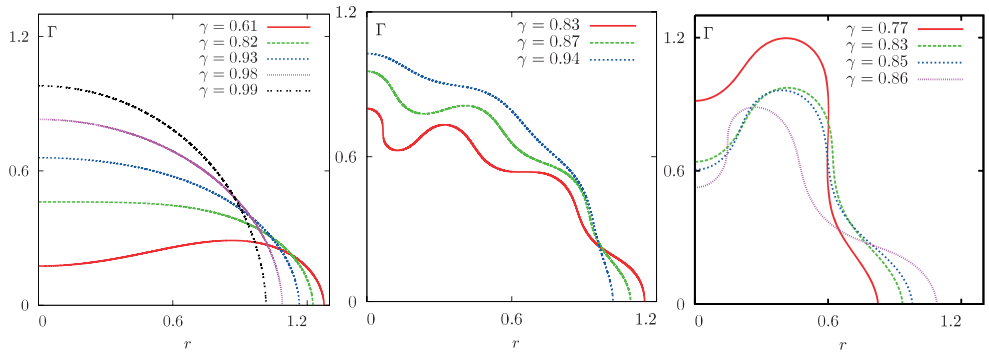

Figure 23. 3D axisymmetric case. (left) Red blood cells (RBCs) shapes having $i^\star \in \{0, 1\}$: the corresponding values of the energy of Canham and Hefrich are, respectively, $\mathcal{J}(\Omega) \in \{55.48, 40.08, 31.24, 28.08, 24.65\}$, from inside to outside. (middle) RBCs shapes having $i^* = 6$: they corresponds respectively to $\mathcal{J}(\Omega) \in \{79.02, 83.23, 84.5, 83.34\}$, from inside to outside. (right) RBCs shapes having $i^\star = 3$: they corresponds respectively to $\mathcal{J}(\Omega) \in \{79.77, 80.47, 80.59, 96.52\}$, from inside to outside.

the computed error $\|\mathscr{H}_\varepsilon(\varphi_{\text{ODE}}) - \mathscr{H}_\varepsilon(\varphi_{\text{h}})\|_{0,2,\Lambda}$ for successively refined meshes with respect to spatial resolution given by the equivalent mesh size h_{eq} defined in Section 4.2.1. The finite element solution is called φ_{h}, whereas φ_{ODE} represents the solution of the reduced order problem. The error history is displayed in Figure 22(right); it depicts the convergence properties and, in particular, the convergence rate of the numerical method. We notice that the error evolution disposes similar convergence rates for the different RBCs. By observing the slope in logarithmic scale, we can suggest that the error convergence follows $\mathcal{O}\left(h^{1+\alpha}\right)$ where $\alpha \in (0, 1)$ represents a real parameter.

4.4. Numerical results in the three-dimensional axisymmetric case

This section is concerned with the numerical investigation of the shapes of RBCs in the three-dimensional case. We aim to give better insight into the properties of the Canham and Helfrich model in the three-dimensional case by further exploring our numerical tools, without the aim of providing a theoretical explanation of the physics underlying. We compute a three-dimensional axisymmetric solution where we assume both a rotational symmetry around the longitudinal axis and a symmetry with respect to the equatorial plane. Therefore, the computational domain covers the fourth of the RBC's shape, while the entire shape is reconstructed by both plannar and rotational symmetries. The modelization of the three-dimensional case with the axisymmetry is motivated by the great geometrical simplifications and the computational gain that one gets by doing two-dimensional computations to model three-dimensional shapes, allowing for an easier understanding of the underlying physics. We notice that the assembly of the global matrices in the three-dimensional axisymmetric case is automatically handled within the finite element environment Rheolef. The reduced order model is briefly described in Appendix B, where we also provide the method used for the numerical approximation. A more detailed study was made by Wan *et al*. [70]. Numerical investigations show that we obtain the usual biconcave shapes of RBCs. Thanks to the simulations, we could bring to light new forms which are, up to our knowledge, unknown in the existing literature.

We focus on the computational domain that corresponds to one-quarter of the equatorial plane. We introduce an integer $i^\star$ that computes the number of point of inflection that corresponds to the points where the concavity changes its sign. In particular, a biconcave shape possess a value $i^\star = 1$, while a sphere possesses a value $i^\star = 0$. We plot in Figure 23 some configurations of the equilibrium of RBCs corresponding to different values of $i^\star \in \{0, 1, 2, 3\}$. All the shapes are dimensionless, and they have a constant surface area equal to 4π. Let us consider, for example, the shapes having $i^\star = 6$: the reduced volume has values close to 1 when the shape is becoming closer to a spherical shape (Figure 23(middle)). We perform a preliminary numerical study using several values of the reduced volume γ. A shape diagram is plotted in Figure 24 where each form of RBCs is represented by a point that the coordinates represent the reduced volume γ and the corresponding energy $\mathcal{J}(\Omega)$, respectively. Numerical results show that a structure of branches is found, and each

DOI: 10.1002/fld

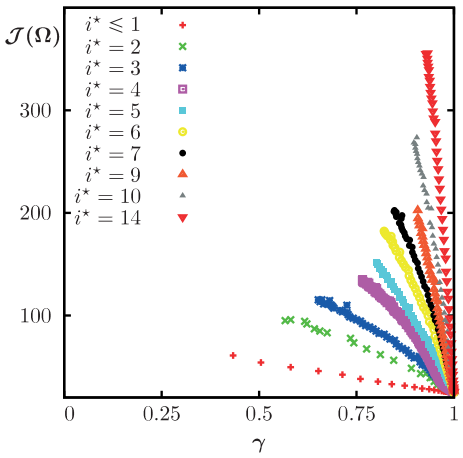

Figure 24. 3D axisymmetric case. Shape diagram of red blood cells showing the Canham–Helfrich energy with respect to γ.

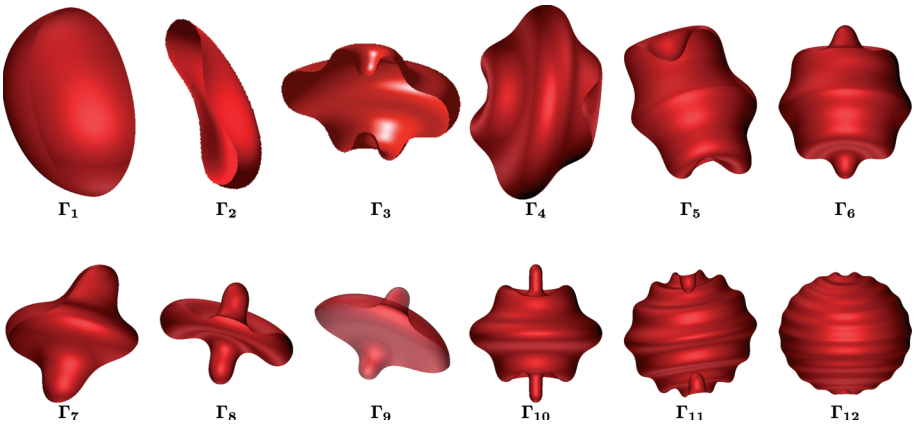

3D axisymmetric shapes			
shape	$i^\star$	γ	$\mathcal{J}(\Omega)$
Γ_1	0	0.91	30.05
Γ_2	1	0.61	55.48
Γ_3	3	0.86	79.77
Γ_4	3	0.84	80.50
Γ_5	3	0.77	96.52
Γ_6	4	0.90	91.90

3D axisymmetric shapes			
shape	$i^\star$	γ	$\mathcal{J}(\Omega)$
Γ_7	2	0.83	50.44
Γ_8	2	0.61	100.61
Γ_9	2	0.79	62.75
Γ_{10}	4	0.78	147.6
Γ_{11}	7	0.89	201.23
Γ_{12}	11	0.94	240.77

Figure 25. 3D axisymmetric case. Overlay of some shapes of red blood cells obtained by the numerical simulations.

branch seems corresponding to fixed value of $i^\star$. Remark that several questions exist with respect to these energy levels, and we need a further study to understand and explain the diagram's structure and, in particular, how the membranes jump between the energy branches. Indeed, we keep varying the reduced volume γ of a RBC initially characterized by a given shape parameter $i^\star$. We observe that a form change occurs when a critical value of γ is reached, and a jump to another energy branch subsequently happens. For a better visual effect, we perform a reconstruction of some three-dimensional shapes, and we give samples of the obtained forms in Figure 25. The values of $i^\star$, γ, and $\mathcal{J}(\Omega)$ characterizing the different RBCs are provided in the table below the shapes. Up to our knowledge, we do not know if some of these forms have been experimentally observed. However, we notice that other non-axisymmetric RBCs shapes obviously exist, but they were not investigated in the present work. An investigation and a stability study of the presented shapes of RBCs will be separately investigated in a forthcoming paper.

DOI: 10.1002/fld

5. CONCLUSIONS

In this paper, we present a mixed finite element method for the simulation of the equilibrium shapes of RBCs following the model proposed by Canham and Helfrich. These configurations are characterized by the minimization of the bending energy under the constraints of fixed volume and surface area. Our derivation is mostly based on a saddle point approach, with a level set method. Our framework allows the use of an anisotropic mesh adaptation technique that helps to better capture the RBC's membrane, and it allows more computational accuracy in the vicinity of the cell. Moreover, our method features the imposition of additional constraints via Lagrange multipliers technique combined with *a posteriori* mass corrections. Numerical results show the robustness of this strategy that enforces the mass preservation and improves the convergence properties of the method. We derive a reduced order model that describes the equilibrium shapes of RBCs in the two-dimensional case and helps to further validate the finite element computations. We present a number of numerical examples in the two-dimensional case and the three-dimensional axisymmetric case that illustrate the main features of the numerical method.

APPENDIX A: REDUCED ORDER MODEL IN THE TWO-DIMENSIONAL CASE

In this appendix, we write a reduced order model that describes the equilibrium state of the red blood cell (RBC) as the solution of an ordinary differential equation (ODE). We assume that the cell is symmetric with respect to the horizontal (i.e., x-axis) and the vertical (i.e., z-axis) axes. The solution of this reduced order model allows to validate the solution of the finite element solver, as depicted in Figure 6.

Notations. Let us consider a functional f that depends on a function $x \to \varphi(x)$. We introduce the notation $f'(x) := \frac{df}{dx}(x)$, and we denote by $D'_\varphi f(\varphi)(\psi)$ the directional derivative of $f(\varphi)$ at φ along the direction ψ.

Mathematical formulation. In the equilibrium state, the RBC is described using a parametric representation $z = h(x)$ (Figure A.1). We denote by x_f the maximum radius of the membrane such that $h(x_f) = 0$. We introduce the function $\phi(x,z) = z - h(x)$. The membrane is then described by $\Gamma = \left\{x \in [0, x_f] \times [0, +\infty] : \phi(x,z) = 0\right\}$. An infinitesimal length on Γ writes $\mathrm{dl} = \sqrt{1 + (h'(x))^2}\mathrm{d}x$, while the area V_0 and the perimeter A_0 reads as follows:

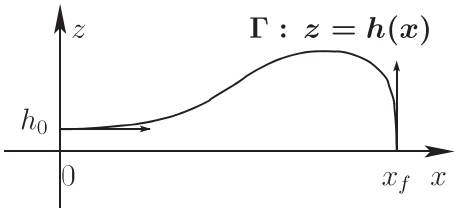

Figure A.1. Cartesian notations used in the two-dimensional case.

$$V_0 = -4\int_0^{x_f} w(x)x\mathrm{d}x \quad \text{and} \quad A_0 = 4\int_0^{x_f} \sqrt{1 + w^2(x)}\mathrm{d}x \qquad \text{with} \qquad w(x) = h'(x). \tag{A.1}$$

Thereafter, we write the problem with respect to w. The normal vector $\mathbf{n}$ and the mean curvature H are given by

$$\mathbf{n}(x) = \frac{\nabla\phi}{|\nabla\phi|} = \frac{1}{\sqrt{1 + w^2(x)}}\begin{pmatrix} -w(x) \\ 1 \end{pmatrix} \quad \text{and} \quad H(x,z) = \nabla.\mathbf{n} = -\frac{w'(x)}{\sqrt{1 + w^2(x)}^3}. \tag{A.2}$$

DOI: 10.1002/fld

The Lagrangian functional writes

$$\frac{\mathcal{L}(\Omega;\lambda,p)}{2}=\int_0^{x_f}\left[(H-H_0)^2+\lambda\right]\sqrt{1+w^2(x)}\mathrm{d}x-2p\int_0^{x_f}xw(x)\mathrm{d}x. \tag{A.3}$$

To write the Euler–Lagrange equation, we look for the saddle points of $\mathcal{L}$ (A.3). We assume that $\psi(x)$ represents a regular function with a compact support. Therefore, we have the following derivatives:

$$D'_w\left[(H-H_0)^2\right](w)(\psi)=2H_\psi(w)(H-H_0),\quad D'_w\left[\sqrt{1+w^2(x)}\right](w)(\psi)=\frac{w(x)\psi}{\sqrt{1+w^2(x)}},\quad \text{and}$$
$$D'_w\mathcal{L}(w;\lambda,p)(\psi)=4\int_0^{x_f}H_\psi(w)(H-H_0)\sqrt{1+w^2(x)}+2\int_0^{x_f}\frac{w\psi\left[(H-H_0)^2+\lambda\right]}{\sqrt{1+w^2(x)}}-4p\int_0^{x_f}x\psi. \tag{A.4}$$

From the expression of H A.2, we obtain

$$H'(x)=-\frac{\left[(1+w(x)^2)w''(x)-3w(x)w'^2(x)\right]}{\sqrt{1+w^2(x)}^5}\quad\text{and}\quad D'_wH(w)(\psi)=-\frac{\psi'(1+w(x)^2)-3w(x)w'(x)\psi}{\sqrt{1+w^2(x)}^5}. \tag{A.5}$$

We denote respectively by T_1, T_2, and T_3 the three terms in the derivative of the Lagrangian (A.4). We have

$$T_1=-\left[\frac{2(H-H_0)}{(1+w(x)^2)}\psi\right]_0^{x_f}+\int_0^{x_f}\frac{\partial}{\partial x}\left[\frac{2(H-H_0)}{(1+w(x)^2)}\right]\psi\mathrm{d}x+\int_0^{x_f}\frac{6w(x)w'(x)(H-H_0)}{(1+w(x)^2)^2}\psi\mathrm{d}x.$$

Because $w(x_f)=-\infty$, we have $\frac{\partial}{\partial x}\left[\frac{2(H(x)-H_0)}{(1+w(x)^2)}\right]=\frac{2H'(x)}{(1+w(x)^2)}-\frac{4(H(x)-H_0)w(x)w'(x)}{(1+w(x)^2)^2}$. Hence, we obtain:

$$T_1=\int_0^{x_f}\frac{2H'(x)}{(1+w(x)^2)}\psi\mathrm{d}x+\int_0^{x_f}\frac{2w(x)w'(x)(H(x)-H_0)}{(1+w(x)^2)^2}\psi\mathrm{d}x. \tag{A.6}$$

From (A.5) and (A.6), we get $\frac{2H'(x)}{(1+w(x)^2)}+\frac{2w(x)w'(x)(H(x)-H_0)}{(1+w(x)^2)^2}=-\frac{2w''(x)}{(1+w(x)^2)^{\frac{5}{2}}}+\frac{4w(x)w'^2(x)}{(1+w(x)^2)^{\frac{7}{2}}}-\frac{2w(x)w'(x)H_0}{(1+w(x)^2)^2}$. By using $(H(x)-H_0)^2+\lambda=\frac{w'(x)^2}{(1+w(x)^2)^3}+\frac{2H_0w'(x)}{(1+w(x)^2)^{\frac{3}{2}}}+\left(H_0^2+\lambda\right)$. We simplify the expression of T_2

$$T_2=\int_0^{x_f}\left[\frac{w(x)w'^2(x)}{(1+w(x)^2)^{\frac{7}{2}}}+\frac{2H_0w'(x)w(x)}{(1+w(x)^2)^2}+\frac{\left(H_0^2+\lambda\right)w(x)}{(1+w(x)^2)^{\frac{1}{2}}}\right]\psi\mathrm{d}x. \tag{A.7}$$

By using T_1 (A.6) and T_2 (A.7), Equation (A.4) reads as follows:

$$D'_w\mathcal{L}(w;\lambda,p)(\psi)=2\int_0^{x_f}\left[-\frac{2w''(x)}{(1+w(x)^2)^{\frac{5}{2}}}+\frac{5w(x)w'^2(x)}{(1+w(x)^2)^{\frac{7}{2}}}+\frac{\left(H_0^2+\lambda\right)w(x)}{(1+w(x)^2)^{\frac{1}{2}}}-2px\right]\psi\mathrm{d}x.$$

DOI: 10.1002/fld

Finally, we obtain the Euler–Lagrange equation for the RBC at equilibrium. The reduced order problem reads as follows:

$$\begin{cases} \dfrac{2w''(x)}{(1+w(x)^2)^{\frac{5}{2}}} = \dfrac{5w(x)w'^2(x)}{(1+w(x)^2)^{\frac{7}{2}}} + \dfrac{\left(H_0^2+\lambda\right)w(x)}{(1+w(x)^2)^{\frac{1}{2}}} - 2px, \quad 0 < x < x_f \\ w(0) = 0 \qquad \text{and} \qquad w'(0) = w_0'. \end{cases} \tag{A.8}$$

Notice that the condition $w_0' > 0$ is needed if we expect a biconcave shape. To decrease the derivation order in (A.8), we consider a variable change $\kappa = w/\sqrt{1+w^2}$, and we write the problem (A.8) with respect to κ. The boundary condition is $\kappa(0) = 0$, and we have $\kappa' = \frac{w'}{\sqrt{1+w^2}^3}$ and $\kappa'' = \frac{w''}{\sqrt{1+w^2}^3} - \frac{3ww'^2}{\sqrt{1+w^2}^5}$. Remark that $\kappa'(0) = w'(0)$. Because both κ and w have the same sign, we obtain $w = \kappa/\sqrt{1-\kappa^2}$. The mean curvature read $H = -\kappa'$. We introduce the polynomial $P(\xi) = \left(H_0^2+\lambda\right)\xi - 2px$. The problem(A.8) writes

$$\kappa'' = \frac{P(\kappa) - \kappa\kappa'^2}{2(1-\kappa^2)} \text{ in } (0, x_f), \qquad \text{with} \quad \kappa(0) = 0 \qquad \text{and} \quad \kappa'(0) = w'(0). \tag{A.9}$$

Numerical discretization. To solve the problem (A.9), the derivation order is first reduced by introducing the variables $y = (y_1, y_2) = (\kappa, \kappa')$, $y_0 = (0, w'(0))$, and $f(y) = \left(y_2\,,\ \dfrac{P(y_1) - y_1 y_2^2}{2\left(1-y_1^2\right)}\right)^T$. A first-order ODE is then obtained $y' = f(y)$ in $(0, x_f)$, and $y(0) = y_0$. We solve the ODE in the interval $[0, x_f]$ with x_f large enough such that $1-\kappa^2(x)$ changes its sign in at a particular value x_c and it becomes negative in the interval (x_c, x_f). A *shooting method* is then needed to obtain the position x_f. Finally, we compute the RBC's shape by $w(x) = \frac{\kappa}{(1-\kappa^2)^{1/2}}$, $0 < x < x_f$, and $h(x) = \int_{x_f}^{x} w(x)\mathrm{d}x$.

APPENDIX B: REDUCED ORDER MODEL IN THE THREE-DIMENSIONAL AXISYMMETRIC CASE

A detailed description of the reduced model in the three-dimensional axisymmetric case is available in [5, 70]. We only present the numerical method. A parametric representation, that is, $z = h(r)$ with $r \in (0, r_f)$, is used to describe the cell membrane, where r is the radial coordinate and z represents the coordinate perpendicular to the equatorial plane. Analogously, a change variable $\kappa(r) = w(r)/r\sqrt{1+w^2(r)}$ allows to describe curvature component coming from the three-dimensional modelization, whereas the mean curvature reads $H(r) = -2\kappa(r) - r\kappa'(r)$. The curvature is singular on the longitudinal axis, and a Taylor expansion around $r = 0$ is then needed. We introduce a small parameter ε, choosen numerically equal to 10^{-7}, and we solve the problem in $[\varepsilon, r_f]$. The ODE reads as follows:

$$\kappa'' = \frac{P(\kappa) - \kappa(r\kappa' + \kappa)^2}{2(1-r^2\kappa^2)} - \frac{3\kappa'}{r}, \text{ for } r \in (\varepsilon, r_f), \qquad \kappa(\varepsilon) = w'(0), \qquad \text{and} \qquad \kappa'(\varepsilon) = 0, \tag{B.1}$$

where $P(\cdot)$ is a given polynomial. Regarding the numerical resolution, we introduce $y = (y_1, y_2)^T = (\kappa, \kappa')^T$ and $f(y, r) = \left(y_2, \frac{P(y_1) - y_1(ry_2+y_1)^2}{2\left(1-r^2y_1^2\right)} - \frac{3y_2}{r}\right)^T$. Let us consider the initial data $y_0 = \left(w_0', 0\right) := (w'(0), 0)$ and the boundary condition at $r = \varepsilon$ given by $y_\varepsilon = \left(w_0', -\varepsilon w_0'^3\right)$. Finally, the problem reads $y' = f(y, r)$ for $r \in (\varepsilon, r_f)$, and $y(\varepsilon) = y_\varepsilon$. Similarly to the two-dimensional Cartesian case, we have

DOI: 10.1002/fld

$$w(r) = \frac{r\kappa}{\sqrt{1 - r^2\kappa^2}}, \quad \text{for } r \in (\varepsilon, r_f) \qquad \text{and} \qquad h(r) = \int_{r_f}^{r} w(r)\mathrm{d}r.$$

ACKNOWLEDGEMENTS

Aymen Laadhari gratefully acknowledges the support by the French National Center for Scientific Research (CNRS) and by the French National Research Agency (ANR MOSICOB) for most of this work, and the support by the Swiss National Science Foundation (grant 320030-149567) at ETH Zürich.

REFERENCES

1. Safran SA. *Statistical Thermodynamics of Surfaces, Interfaces and Membranes*, Frontier in Physics, vol. 90. Addison-Wesley Publishing Company: Reading, MA, 1994.
2. Biben T, Kassner K, Misbah C. Phase-field approach to three-dimensional vesicle dynamics. *Physical Review E* 2005. 72:041921-1-041921-15.
3. Kaoui B, Ristow GH, Cantat I, Misbah C, Zimmermann W. Lateral migration of a two-dimensional vesicle in unbounded poiseuille flow. *Physical Review E* 2008; **77**:021903.
4. Seifert U. Configurations of fluid membranes and vesicles. *Advances in Physics* 1997; **46**:13–137.
5. Au TKK, Wan TYH. Analysis on an ODE arisen from studying the shape of a red blood cell. *Journal of Mathematical Analysis and Applications* 2003; **282**(1):279–295.
6. Bonito A, Nochetto RH, Pauletti MS. Dynamics of biomembranes: effect of the bulk fluid. *Mathematical Modelling of Natural Phenomena* 2011; **6**:25–43.
7. Elschner J, Pozrikidis C. Boundary integral and singularity methods for linearized viscous flow. Cambridge University Press 1992. *Journal of Applied Mathematics and Mechanics* 1994; **74**(2):104–104.
8. Veerapaneni SK, Gueyffier D, Zorin D, Biros G. A boundary integral method for simulating the dynamics of inextensible vesicles suspended in a viscous fluid in 2D. *Journal of Computational Physics* 2009; **228**(7):2334–2353.
9. Dziuk G. Computational parametric Willmore flow. *Numerische Mathematik* 2008; **111**(1):55–80.
10. Sachse FB. *Computational Cardiology: Modeling of Anatomy, Electrophysiology, and Mechanics*. Springer-Verlag: Berlin, 2004.
11. Deuling H, Helfrich W. Red blood cell shapes as explained on the basis of curvature elasticity. *Biophysical Journal* 1976; **16**:861–868.
12. Deuling HJ, Helfrich W. A theoretical explanation for the myelin shapes of red blood cells. *Blood Cells* 1977; **3**: 713–720.
13. Hu J, Ou-Yang Z. Shape equations for the axisymmetric vesicles. *Physical Review E* 1993; **47**:461–467.
14. Laadhari A, Saramito P, Misbah C. Computing the dynamics of biomembranes by combining conservative level set and adaptive finite element methods. *Journal of Computational Physics* 2014; **263**(0):328–352.
15. Zheng WM, Liu J. Helfrich shape equation for axisymmetric vesicles as a first integral. *Physical Review E* 1993; **48**(4):2856–2860.
16. Julicher F, Seifert U. Shape equations for axisymmetric vesicles: a clarification. *Physical Review E* 1994; **49**(5): 4728–4731.
17. Hu ZN. New approach on the general shape equation of axisymmetric vesicles. *Modern Physics Letters B* 1999; **13**(1):13–18.
18. Veerapaneni SK, Raj R, Biros G, Purohit PK. Analytical and numerical solutions for shapes of quiescent 2D vesicles. *International Journal of Non-Linear Mechanics* 2009; **44**(3):257–262.
19. Canham PB. The minimum energy of bending as a possible explanation of the biconcave shape of the human red blood cell. *Journal of Theoretical Biology* 1970; **26**:61–81.
20. Helfrich W. Elastic properties of lipid bilayers: theory and possible experiments. *Zeitschrift Fur Naturforschung Section C* 1973; **28**:693–703.
21. Ou-Yang ZC, Helfrich W. Bending energy of vesicle membranes: general expressions for the first, second and third variation of the shape energy and applications to spheres and cylinders. *Physical Review A* 1989; **39**(10):5280–5288.
22. Bryant RL. A duality theorem for Willmore surfaces. *Journal of Differential Geometry* 1984; **20**(1):23–53.
23. Willmore TJ. *Riemannian Geometry*. Clarendon: Oxford, 1993.
24. Walani N, Torres J, Agrawal A. Anisotropic spontaneous curvatures in lipid membranes. *Physical Review E* 2014; **89**:062715.
25. Laadhari A, Saramito P, Misbah C. Vesicle tumbling inhibited by inertia. *Physics of Fluids* 2012; **24**:031901.
26. Du Q, Liu C, Wang X. A phase field approach in the numerical study of the elastic bending energy for vesicle membranes. *Journal of Computational Physics* 2004; **198**:450–468.
27. Du Q, Li M, Liu C. Analysis of a phase Field Navier–Stokes vesicle–fluid interaction model. *Discrete and Continuous Dynamical System – Series B* 2007; **8**:539–556.
28. Seifert U, Berndl K, Lipowsky R. Shape transformations of vesicles: phase diagram for spontaneous-curvature and bilayer-coupling models. *Physical Review A* 1991; **44**:1182–1202.
29. Banham T, Li B, Zhao Y. Pattern formation by phase-field relaxation of bending energy with fixed surface area and volume. *Physical Review E* 2014; **90**:033308.

DOI: 10.1002/fld

30. Zhong-Can OY, Helfrich W. Bending energy of vesicle membranes: general expressions for the first, second and third variation of the shape energy and applications to spheres and cylinders. *Physical Review A* 1989; **39**(10):5280–5288.
31. do Carmo MP. *Differential Geometry of Curves and Surfaces*. Prentice-Hall: Englewood Cliffs, NJ, 1976.
32. Simon J. Differentiation with respect to the domain in boundary value problems. *Journal of Numerical Functional Analysis and Optimization* 1980; **2**(7–8):649–687.
33. Allaire G, Jouve F. Minimum stress optimal design with the level set method. *International Journal of Boundary Elements and Applications* 2008; **32**:909–918.
34. Laadhari A, Misbah C, Saramito P. On the equilibrium equation for a generalized biological membrane energy by using a shape optimization approach. *Physica D* 2010; **239**:1567–1572.
35. Du Q, Liu C, Wang X. Simulating the deformation of vesicle membranes under elastic bending energy in three dimension. *Journal of Computational Physics* 2006; **212**:757–777.
36. Cristini V, Bawzdziewicz J, Loewenberg M. Drop breakup in three-dimensional viscous flows. *Physics of Fluids* 1998; **10**:1781–1783.
37. Khayat RE. Three-dimensional boundary-element analysis of drop deformation for Newtonian and viscoelastic systems. *International Journal for Numerical Methods in Fluids* 2000; **34**:241–275.
38. Peskin CS. The immersed boundary method. *Acta Numerica* 2002; **11**:1–39.
39. Zhao L, Bai X, Li T, Williams JJR. Improved conservative level set method. *International Journal for Numerical Methods in Fluids* 2014; **75**(8):575–590.
40. Gueyffier D, Li J, Nadim A, Scardovelli R, Zaleski S. Volume-of-fluid interface tracking with smoothed surface stress methods for three-dimensional flows. *Journal of Computational Physics* 1999; **152**:423–456.
41. Menard T, Tanguy S, Berlemont A. Coupling level set/VOF/ghost fluid methods: Validation and application to 3D simulation of the primary break-up of a liquid jet. *International Journal of Multiphase Flow* 2007; **33**(5):510–524.
42. Allen SM, Cahn JW. A microscopic theory for antiphase boundary motion and its application to antiphase domain coarsening. *Acta Metallurgica* 1979; **27**:1085–1095.
43. Du Q, Liu C, Ryham R, Wang X. Energetic variational approaches in modeling vesicle and fluid interactions. *Physica D: Nonlinear Phenomena* 2009; **238**(9–10):923–930.
44. Osher S, Sethian JA. Fronts propaging with curvature depend speed: Algorithms based on Hamilton-Jacobi formulations. *Journal of Computational Physics* 1988; **79**(1):12–49.
45. Osher S, Fedkiw R. Level Set methods: An overview and some recent results. *Journal of Computational Physics* 2001; **169**(2):463–502.
46. Cottet GH, Maitre E, Milcent T. Eulerian formulation and level-set models for incompressible fluid-structure interaction. *Mathematical Modeling and Numerical Analysis* 2008; **42**:471–492.
47. Laadhari A, Saramito P, Misbah C. Improving the mass conservation of the level set method in a finite element context. *Comptes Rendus Mathematique Serie I* 2010; **348**:535–540.
48. Salac D, Miksis M. A level set projection model of lipid vesicles in general flows. *Journal of Computational Physics* 2011; **230**:8192–8215.
49. Murat F, Simon J. Quelques résultats sur le contrôle par un domaine géométrique. *Technical Report LA 189*, Lab. d'Analyse Numérique, Univ. Paris VI, 1974.
50. Allaire G, Jouve F, Toader AM. Structural optimization using sensitivity analysis and a level-set method. *Journal of Computational Physics* 2004; **194**(1):363–393.
51. Evans YC, Spruck J. Motion of level sets by mean curvature. *Journal of Differential Geometry* 1991; **33**(8):635–681.
52. Borouchaki H, George PL, Mohammadi B. Delaunay mesh generation governed by metric specifications part II. Applications. *Finite Elements in Analysis and Design* 1997; **25**:85–109.
53. George PL, Borouchaki H. *Triangulation de delaunay et maillage: applications à la méthode des éléments finis*. Hermes, Paris, 1997.
54. Hecht F. A few snags in mesh adaptation loops. In *Proceedings of the 14th International Meshing Roundtable*. Springer: Berlin Heidelberg, 2015; 301–313.
55. Huang W, Li X. An anisotropic mesh adaptation method for the finite element solution of variational problems. *Finite Elements in Analysis and Design* 2010; **46**:61–73.
56. Kamenski L, Huang W. How a nonconvergent recovered Hessian works in mesh adaptation. *SIAM Journal on Numerical Analysis* 2014; **52**(4):1692–1708.
57. Golub GH. *Matrix Computations* (3rd Edition), Vol. 10. Johns Hopkins University Press: Baltimore, 1996.
58. Golub GH, Reinsch C. Singular value decomposition and least squares solutions. *Numerische Mathematik* 1970; **14**(5):403–420.
59. Golub G, Kahan W. Calculating the singular values and pseudo-inverse of a matrix. *SIAM Journal on Numerical Analysis* 1965; **2**(2):205–224.
60. Arrow J, Hurwicz L, Uzawa H. Studies in linear and nonlinear programming. Stanford University Press, 1958.
61. Fortin M, Glowinski R. méthodes de lagrangien augmenté. applications à la résolution numerique de problames aux limites. Number 9 in Méthodes mathématiques de l'informatique. Dunod, Paris, 1982.
62. Glowinski R. *Numerical Methods for Nonlinear Variational Problems*. Springer-Verlag: New York, 1984.
63. Glowinski R, Le Tallec P. *Augmented Lagrangians and Operator-splitting Methods in Nonlinear Mechanics*. SIAM: Philadelphia, 1989.
64. Saramito P. *Efficient c++ Finite Element Computing with Rheolef*. CNRS-CCSD Ed., Paris, 2014.

DOI: 10.1002/fld

65. Eaton JW, Bateman D, Hauberg S. *GNU Octave Version 3.0.1 Manual: A High-Level Interactive Language for Numerical Computations*. Create Space Independent Publishing Platform ISBN:1441413006, 2009. [www.gnu.org/software/octave], 2009.
66. Zalesak S. Fully multidimensional flux-corrected trasport algorithms for fluids. *Journal of Computational Physics* 1979; **31**:335–362.
67. Zhang D, Jiang C, Liang D, Chen Z, Yang Y, Shi Y. A refined volume-of-fluid algorithm for capturing sharp fluid interfaces on arbitrary meshes. *Journal of Computational Physics* 2014; **274**(0):709–736.
68. Leveque RJ. High-resolution conservative algorithms for advection in incompressible flow. *SIAM Journal of Numerical Analysis* 1996; **33**:627–665.
69. Enright D, Fedkin R, Ferziger J, Mitchell I. A hybrid particle level set method for improved interface capturing. *Journal of Computational Physics* 2002; **183**:83–116.
70. Au TK-K, Wan TY-H. Analysis on an ODE arisen from studying the shape of a red blood cell. *Journal of Mathematical Analysis and Applications* 2003; **282**(1):279–295.

DOI: 10.1002/fld